

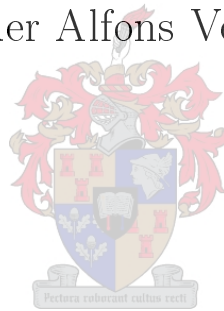


UNIVERSITEIT•STELLENBOSCH•UNIVERSITY
jou kennisvenoot • your knowledge partner

The design of a dual reflector feed using surrogate modeling techniques.

by

Alexander Alfons Vermeulen



*Report submitted in partial fulfilment of the requirements for
the degree Masters in Engineering in the Department of
Electrical and Electronic Engineering at the University of
Stellenbosch*

Study leader: Dr. D. de Villiers

March 2016

Acknowledgements

I would like to extend the utmost gratitude to the following people and organisations:

My supervisor Dr. D. de Villiers for his guidance, patience, and support throughout.

SKA SA for their financial support that made this thesis possible.

Mr. J de Klerk for providing some 11th hour translations.

Declaration

By submitting this thesis electronically, I declare that the entirety of the work contained therein is my own, original work, that I am sole author thereof (save to the extent explicitly otherwise stated), that reproduction and publication thereof by Stellenbosch University will not infringe any third party rights and that I have not previously in its entirety or in part submitted it for obtaining any qualification.

March 2016

Copyright ©2016 Stellenbosch University

All rights reserved

Summary

The optimisation of a feed horn for a dual Gregorian reflector antenna system using surrogate modelling was investigated. This included a brief overview of dual reflector antenna systems as well as their performance parameters. The design for a three axial choke horn with a variety of matching sections was described for use with the optimisation. Two techniques were investigated, namely space mapping (SM) and a Kriging interpolate based approach. The SM technique consisted of augmenting a fast coarse model by aligning it to a slow fine model. This showed potential but was ultimately hampered by the lack of a coarse model that did not require a full wave simulation for the primary feed pattern and so was abandoned. The interpolation based technique could use two approaches. The first consisted of an interpolate based on a coarse data set that was then corrected using a regression model based on the difference between the fine and coarse model at a few training sites. The second approach consisted of only an interpolate that was based on a fine data set. The technique was applied to a multi-objective optimisation (MOO) problem. The optimisation aimed at minimizing the reflection coefficient and maximizing the sensitivity of the reflector system. It was shown to work well and produced reasonably accurate results while reducing the total optimisation time from potentially weeks or months down to the order of a day. As part of the investigation an MOO algorithm called multi-objective population based incremental learning (MOPBIL) was implemented. The basic concepts of MOO and MOPBIL were discussed and the implementation was described. This implementation was also fully tested and shown to approximate the Pareto front well.

Opsomming

Die optimering van 'n voerhoering vir 'n dubbelweerkatser Gregoriaanse antennastelsel wat gebruik maak van 'n surrogaat model was geondersoek. Dit het 'n kort oorsig ingesluit van die dubbelweerkatser antennastelsels asook die prestasie grense daarvan.

Die ontwerp van 'n horing antenna met drie aksiale smoorder, vir verskeie tipes aanpassingseksies, is beskryf vir gebruik in die optimeringstrategie. Twee tegnieke was ondersoek, naamlik spasie kartering (SK) en 'n Kriging interpolasie-gebaseerde benadering. Die SK tegniek het bestaan uit die verfyning van 'n vinnige growwe model deur die aanpassing daarvan na 'n stadige fyn model. Dit het potensiaal getoon, maar is uiteindelik laat vaar as gevolg van 'n gebrek aan 'n growwe model wat nie 'n volgolf simulasie vir die primêre voer patroon benodig nie. Die interpolasie gebaseerde tegniek kon twee benaderings gebruik. Die eerste het bestaan uit 'n interpolasie gebaseer op 'n growwe datastel wat dan reggestel was met behulp van 'n regressiemodel gebaseer op die verskil tussen die fyn en growwe model soos gevind by 'n paar opleidingspunte. Die tweede benadering het slegs bestaan uit 'n interpolasie wat gebaseer was op 'n fyn datastel. Die tegniek was toegepas op 'n multi-doel optimeringsprobleem (MO). Die optimering was gemik daarop om die stelsel se weerkaatsings-koëffisiënt te minimeer sowel as om die sensitiwiteit te maksimeer. Die laasgenoemde benadering het aanduiding gegee dat dit goed werk deur redelike akkurate resultate te lewer terwyl die totale optimeringstyd van moontlike weke of maande na so min as 'n dag verminder was. As deel van die ondersoek was 'n MO algoritme wat bekend staan as 'Multi-objective population based incremental learning' (MOPBIL) geïmplementeer. Die basiese konsepte van MO en MOPBIL was bespreek en die implementering was beskryf. Hierdie implementering was ook ten volle getoets en resultate het gewys dat dit die Pareto front goed benader.

Contents

Acknowledgements	i
Declaration	ii
Summary	iii
Opsomming	iv
Contents	v
List of Figures	viii
List of Tables	xii
1 Introduction	1
2 Reflector Antenna Design	3
2.1 Introduction	3
2.2 Reflector Antennas	3
2.2.1 Dual Offset Reflector Antennas	4
2.2.2 Physical Parameters	5
2.2.3 Feed Horn	6
2.3 Sensitivity	9
2.3.1 Effective Aperture	9
2.3.2 Total System Noise Temperature	14
2.4 Side Lobe Level	16
3 Space Mapping	17
3.1 Introduction	17
3.2 Fundamental Concept	17
3.2.1 Input SM	18
3.2.2 Output SM	18
3.2.3 Implicit SM	19

<i>CONTENTS</i>	vi
3.2.4 Generalized Implicit Space Mapping	19
3.2.5 Single-Objective optimisation using SM	20
3.3 Application to Reflector Feed Design	21
3.3.1 Experimental Design	21
3.3.2 Results	22
3.3.3 Challenge of Applying SM	23
4 Multi-objective optimisation	25
4.1 Introduction	25
4.2 Fundamental Concept	25
4.2.1 Single- vs. Multi-objective optimisation	26
4.2.2 Important Features of a MOO	27
4.3 Implementation	28
4.3.1 PBIL	28
4.3.2 MOPBIL	29
4.3.3 Unique to the Implementation	30
4.4 Testing the Implementation	31
4.4.1 The test functions	31
4.4.2 Results	35
5 Multi-objective Feed Design	38
5.1 Introduction	38
5.2 Surrogate Model	38
5.2.1 General Procedure for Model Construction	39
5.3 Feed 2: Three chokes with a step	43
5.3.1 Probing the Solution Space	44
5.3.2 Characterizing the Objective Space	45
5.3.3 Optimisation Results	46
5.3.4 Case study	49
5.4 Feed 3: Three chokes with a linear taper	52
5.4.1 Two dimensional solution space	53
5.4.2 Three dimensional solution space	56
5.4.3 Case Studies	58
5.4.4 Conclusion	61
6 Discussion	64
List of References	66
Appendix Appendix	68

<i>CONTENTS</i>	vii
Appendix A Tables	69
Appendix B Feed Profiles	71

List of Figures

2.1	Diagram of the x-z profile of an offset Gregorian antenna with a few relevant parameters. The x and z axes are the main reflector axis system while the z_{sr} axis is part of the sub-reflector axis system. The blue circle marks the primary focus while the red circle marks the secondary focus. The dotted lines are ray traces, while the red crosses mark the edges and centre of the main- and sub-reflector	5
2.2	Original design diagram for axially corrugated horn. [1]	6
2.3	Modified axial corrugated horn design diagram	6
3.1	High level diagram of SM optimisation cycle.	20
3.2	The horn profile used for the SM investigation with three chokes and no matching section.	21
3.3	These figures show the results of the experiment while using SM parameter A . The responses over flare angle are shown in (a) with R_f (blue solid line), R_c (red dashed line), and R_s (black crosses) while the value of the SM parameter A used for R_s at each point is shown in (b).	22
3.4	These figures show the results of the experiment while using SM parameter c . The responses over flare angle are shown in (a) with R_f (blue solid line), R_c (red dashed line), and R_s (black crosses) while the value of the SM parameter c used for R_s at each point is shown in (b).	23
4.1	Diagram of a two dimensional space with three example points y_1 , y_2 , and y_3 . The additional arrows next to the axes show the direction of improvement for the purposes of Pareto dominance.	27
4.2	High level diagram of the MOPBIL implementation.	29
4.3	MOPBIL and random search results on test functions \mathcal{T}_1 to \mathcal{T}_6	36
5.1	Example of different model elements constituting the sensitivity model. The reflection coefficient model would only consist of (c) and be constructed from (a)	40

5.2	A one dimensional example of the realignment. (a) shows the unaligned model and (b) shows the aligned model. The red dotted line shows the interpolate through the coarse data points marked as red circles. The back circles represent fine training data and the black line is the surrogate response curve consisting of the interpolate and the regression model. The red and black diamonds represent coarse and fine validation data respectively.	43
5.3	Second feed topology with three chokes and a single step	43
5.4	Diagram showing the sampling strategy for the initial probe of the solution space.	44
5.5	This shows the mean sensitivity along the three central axes of the solution space (a) θ_{flare} , (b) D_F , and (c) L_f . The red squares show fine model evaluations while the black dots are coarse model evaluations.	45
5.6	The maximum reflection coefficient across frequency along each of the three central axes (a) θ_{flare} , (b) D_F , and (c) L_f of the solution space.	45
5.7	(a) The sensitivity surrogate response surface for stepped horn profile is shown by the surface. The black dots show the original coarse data while the fine training data is shown by the red circles. (b) The response surface of the regression model to correct some of the coarse data error.	46
5.8	The reflection coefficient surrogate (maximum over frequency) response surface for second horn is shown as the surface. The green dots show the mean over frequency of the reflection coefficient calculated from the original frequency dependant coarse data set. The two plots are identical, only with different orientations.	47
5.9	Optimisation results for the stepped horn profile with (a) the Pareto front and (b) the Pareto set. Black dots show the surrogate results while the red circles show the solutions chosen for validation.	48
5.10	The Pareto set plotted as (a) black dots on the sensitivity response surface and (b) as grey dots on the reflection coefficient response surface. The red circles in both represent the validation set.	49
5.11	The Pareto set plotted onto the (a) SLL_1 interpolate response surface as grey dots and (b) SLL_2 interpolate response surfaces as black dots. Both the SLL_1 and SLL_2 values are averages over frequency.	49
5.12	The solid lines with markers show the sensitivity over frequency for the three solution in Table 5.1. The dashed lines show the mean values that would be used by the surrogate. The black traces refer to the S_1 , the red to the C_1 , and the green to the M_1	51
5.13	The solid lines plot the reflection coefficient over frequency. The dashed lines show the maximum values that would be used by the surrogate. The black traces refer to the S_1 , the red to the C_1 , and the green to the M_1	51

5.14	Maximum gain over frequency of the primary pattern generated by the three example solutions. The black trace refers to S_1 , the red to C_1 , and the green to the M_1	52
5.15	Aperture efficiency over frequency for the whole reflector system. The black trace refers to S_1 , the red to C_1 , and the green to M_1	52
5.16	Antenna temperature averaged over tipping angle versus frequency for the whole reflector system. The black trace refers to S_1 , the red to C_1 , and the green to M_1	52
5.17	SLL ₁ over frequency of the secondary pattern. The black trace refers to S_1 , the red to C_1 , and the green to M_1	52
5.18	SLL ₂ over frequency of the secondary pattern. The black trace refers to S_1 , the red to C_1 , and the green to M_1	52
5.19	Third feed topology with three chokes and a linear taper	53
5.20	The Pareto front plotted as black dots for the tapered profile with a two dimensional solution space. The validation set is mark by red circles.	54
5.21	The Pareto set plotted as black dots for the tapered profile with a two dimensional solution space. The validation set is mark by red circles.	54
5.22	(a) The Pareto set plotted as black dots onto the sensitivity response surface of the tapered profile with a two dimensional solution space. The validation set is mark by red circles. (b) The response surface of the regression model used to correct some of the coarse model errors.	55
5.23	The Pareto set plotted as black dots onto the reflection coefficient response surface of the tapered profile with a two dimensional solution space. The validation set is mark by red circles.	55
5.24	The Pareto set plotted as black dots onto the SLL ₁ response surface of the tapered profile with a two dimensional solution space. The validation set is mark by red circles.	56
5.25	The Pareto set plotted as black dots onto the SLL ₂ response surface of the tapered profile with a two dimensional solution space. The validation set is mark by red circles.	56
5.26	The Pareto front from the optimisation of the tapered profile with a three dimensional solution space represented as black dots. The red circles show the validation set.	57
5.27	The Pareto set from the optimisation of the tapered profile with a three dimensional solution space shown as black dots. The validation set is represented by red circles.	57

5.28	The reflection coefficient over frequency is shown for (a) the two dimensional solutions and (b) the three dimensional solutions. The best sensitivity solutions S_2 and S_3 are represented by black traces while the compromise solutions C_2 and C_3 are represented by red traces and the best match solution M_2 and M_3 are represented by green traces. The solid line represent the frequency response while the dashed lines show the simplified surrogate response (maximum over frequency) for the solutions.	58
5.29	The sensitivity over frequency is shown for (a) the two dimensional solutions and (b) the three dimensional solutions. The best sensitivity solutions S_2 and S_3 are represented by black traces while the compromise solutions C_2 and C_3 are represented by red traces and the best match solution M_2 and M_3 are represented by green traces. The solid line represent the frequency response while the dashed lines show the simplified surrogate response (mean over frequency) for the solutions.	59
5.30	Above is shown maximum gain over frequency of the primary feed patter for (a) the two and (d) the three dimensional solutions. The aperture over frequency efficiency of the whole reflector system for (b) the two and (e) three dimensional solutions and the antenna temperature over frequency for (c) the two and (f) three dimensional solutions are also shown. The best sensitivity solutions S_2 and S_3 are represented by black traces while the compromise solutions C_2 and C_3 are represented by red traces and the best match solution M_2 and M_3 are represented by green traces.	60
5.31	The SLLs over frequency of the secondary pattern for both two and three dimensional example solutions are shown. (a) SLL_1 and (b) SLL_2 of the two dimensional solutions. (c) SLL_1 and (d) SLL_2 of the three dimensional solutions. The best sensitivity solutions S_2 and S_3 are represented by black traces while the compromise solutions C_2 and C_3 are represented by red traces and the best match solution M_2 and M_3 are represented by green traces. . .	61
B.1	Stepped profile examples from the two dimensional validation set in Section 5.3.3.	71
B.2	Tapered profile examples from the two dimensional validation set in Section 5.4.1	71
B.3	Tapered profile examples from the three dimensional validation set in Section 5.4.2	71

List of Tables

2.1	The reflector specifications used for this study	6
5.1	Three stepped profile solutions chosen from the validation set in Table A.2 for further investigation. The short hand for each solution is indicated in brackets.	50
5.2	Three tapered profiles chosen from the two dimensional validation set, shown in Table A.3, for further investigation. The short hand for each solution is indicated in brackets.	58
5.3	Three tapered profiles chosen from the three dimensional validation set, shown in Table A.4, for further investigation. The short hand for each solution is indicated in brackets.	58
A.1	Default horn parameters with all factors set to 1.	69
A.2	Validation set results for the two dimensional solution space optimisation of the stepped horn from Section 5.3.3.	69
A.3	Validation set results for the two dimensional solution space optimisation of the tapered horn from Section 5.4.1.	70
A.4	Validation set results for the three dimensional solution space optimisation of the tapered horn From Section 5.4.2.	70

Chapter 1

Introduction

In modern antenna design, numerical optimisation is a fundamental part of the process.

Numerical optimisation is, by nature, an iterative process that requires many evaluations of some numerical model representing the system. The problem is that all too often these models are computationally expensive which translates to the optimisation taking a very long time or simply not being at all feasible. An obvious solution to this is to simply reduce the number of evaluations needed and much work has been done on refining optimisation algorithms [2]. The issue is that, though reduced, large numbers of model evaluations are still generally required. A second obvious solution is to use faster models. This has a major drawback in that these generally gain speed at the expense of accuracy. A possible answer to this is to use a technique called surrogate modelling. In basic terms surrogate modelling refers to the concept of using one or more existing models to create a new, or surrogate, model. The power of this technique is that the information present in the existing models can often be more efficiently used making the surrogate model faster or more accurate than the models they were based on. For instance a slow but accurate model could be used to make a fast approximate model more accurate.

The focus of this study was to apply some of these surrogate modelling techniques to the design of a feed antenna for a dual Gregorian reflector system. Two approaches were investigated, namely Space mapping (SM) and a Kriging interpolation based technique. SM was proposed by Bandler et al [3] and refers to a technique that aims to reduce the inaccuracy of a fast coarse model by borrowing information from a slow but accurate fine model. Kriging interpolation was originally proposed by Krige [4] and is a well established technique for building continuous models from discrete data. Using this, a fast surrogate model can be constructed from a slow accurate model by sampling its response over a parameter space. Ideally the surrogate will retain most of the fine model's accuracy while being very quick to evaluate.

Initially, aspects of dual reflector antenna systems were studied in terms of system geometry, feed profile, and performance parameters. The viability of SM was then investigated by applying it to modelling the aperture efficiency of a dual reflector system given a particular feed with the aim of applying it to a single-objective optimisation (SOO). This used a well established closed form approximation as a coarse model and a full wave simulation as the fine model.

The Kriging interpolation based technique was then investigated for use in a multi-objective optimisation (MOO). Prior to this a MOO algorithm called multi-objective population based incremental learning (MOPBIL) was implemented for use as the optimizer. The implementation was based on a SOO algorithm known as population based incremental learning (PBIL). With the optimizer implemented, two forms of the surrogate model were used. The first modelled the reflection coefficient of the feed horn and used only an interpolate through the data from a full wave simulation.

The second modelled the sensitivity of the reflector system and used an interpolate through a set of coarse data based on an antenna noise temperature approximation technique. It was then augmented using a regression model based on the error between this coarse data and fine data from a full secondary pattern noise integration at a small number of training points. Two horn profiles are optimised and the Pareto set extracted using two and three dimensional parameter spaces. The results were then discussed by comparing examples chosen from the Pareto sets.

The results from the optimisation showed that the surrogate maintained errors below 1 % for both the two and three dimensional parameter spaces with no need for realignment. At most approximately a day of simulation was required to build each surrogate and the optimisation took on the order of minutes to run. This contrasted strongly with estimates of the order of weeks or months if the models were evaluated directly. The examples showed good performance similar to that seen in previous work [5].

Chapter 2

Reflector Antenna Design

2.1 Introduction

It is important to first elaborate on some the fundamental concepts related to reflector antenna systems. To this effect a short description of reflector antennas, in particular dual offset reflector antennas, will be given. The general structure of an axial choke horn design for use as the feed will then be described in detail. Particular attention will be paid to the design parameters. Finally a few relevant performance parameters will be discussed.

2.2 Reflector Antennas

A reflector antenna is a system that uses one or more conducting surfaces to shape an existing feed, or primary, radiation pattern to produce a new, or secondary, pattern.

Reflector antennas encompass a wide range of feed antennas, reflector shapes, and overall configurations. One of the most common reflector antennas in use is the parabolic reflector antenna. The reason for this is that a parabolic profile is very good at collimating the primary pattern and producing a high gain secondary pattern. This is due to the property of parabola that any ray travelling parallel to focal axis of the parabola that is incident on the parabola will be reflected towards the focus. Similarly, any ray originating from the focus that is incident on the parabola is reflected into a path parallel to the focal axis.

2.2.1 Dual Offset Reflector Antennas

For additional design freedom a second reflector, or sub-reflector, can be added to form a dual reflector system. A commonly used configuration, call a dual Gregorian reflector antenna, uses an ellipsoidal sub-reflector with a paraboloidal main reflector because an ellipsoid has two focal points and the property that if a ray originates from one focus and is incident on the ellipsoid it will be reflected towards the other focus. Additionally the distance travelled by all such rays from one focus to the other would be identical.

This means that a feed pattern centred at one focus of an ellipsoidal reflector can be made to look as though it is centred at the other focus. So if the second focus is then aligned with the focus of a main paraboloidal reflector, or prime focus, it functions exactly as if a feed pattern had been placed at the prime focus.

This means that the feed antenna no longer needs to be positioned at the prime focus. Construction and maintenance of the antenna can benefit from this because now the feed antenna and the accompanying electronics can be placed in a more accessible position for cabling and personal. Another important use is that it partially decouples the overall size of the antenna system from the effective F/D_m ratio of the antenna system.

The F/D_m ratio refers to the ratio of the focal length F to the diameter D_m of the projected aperture of the main reflector. The projected aperture, or simply aperture, refers to the projection of the main reflector onto a plane perpendicular to the focal axis. The F/D_m ratio plays an important role in antenna performance but also determines how far from the main dish the feed should lie given a specific aperture size. The problem is that a desired F/D_m ratio could mean an impractical antenna configuration. The use of a sub-reflector can remedy this because Rusch et al [6] showed that, for a given Gregorian antenna, there is an equivalent single paraboloidal antenna with an identical aperture but a different focal length to that of the main reflector of the the dual Gregorian antenna.

Another problem for reflector antennas with paraboloidal main reflectors is that the focal point sits in the path of the main beam. This means that either the feed antenna or the sub-reflector as well as the accompanying support structures will cause blockages. This can be overcome by using an asymmetrical section of the paraboloid that does not include the vertex. The beam is still formed parallel to the focal axis but is shifted away from the axis. This does come at the cost of increase cross-polarisation as the field is no longer reflected symmetrically. Usefully, this cross-polarisation can be eliminated by using a dual reflector system and satisfying the Mizugutch criterion [7].

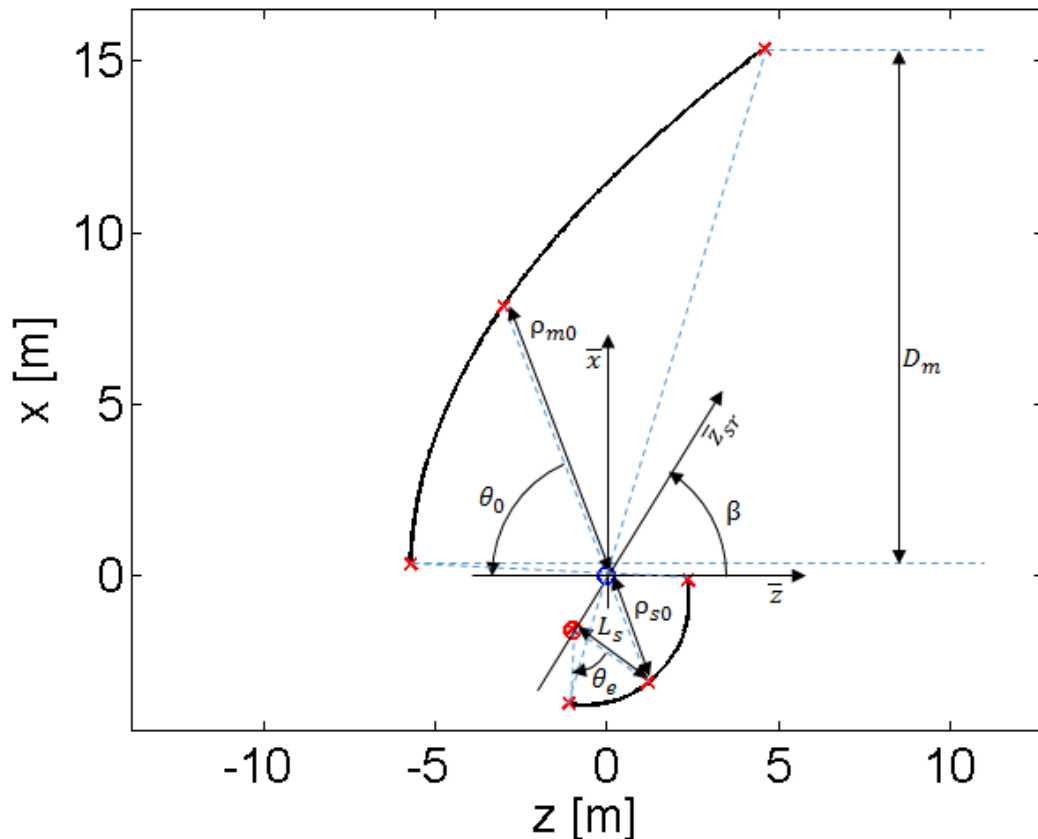


Figure 2.1: Diagram of the x-z profile of an offset Gregorian antenna with a few relevant parameters. The x and z axes are the main reflector axis system while the z_{sr} axis is part of the sub-reflector axis system. The blue circle marks the primary focus while the red circle marks the secondary focus. The dotted lines are ray traces, while the red crosses mark the edges and centre of the main- and sub-reflector

2.2.2 Physical Parameters

Dual Gregorian reflector systems are geometrically complex systems with a large number of potential design parameters. Granet [8] lists 21 design parameters that are spread over three different axes. These parameters contain a high degree of codependency however and Granet went on to show that a dual reflector system, that satisfies the Mizugutch condition, can be fully specified using only five of the 21 design parameters.

The five parameters used to define the reflector system for this study are shown in Figure 2.1. These are the aperture diameter D_m , the half subtended angle between the feed and sub-reflector θ_e , distance from the feed to the centre of the sub-reflector L_s , the tilt angle between the main-reflector and sub-reflector axis systems β , and the angle between the negative z axis and the centre of the main-reflector θ_0 . The values used are shown in Table 2.1.

The additional terms ρ_{m0} and ρ_{s0} in Figure 2.1 are the distance from the primary focus to the centre of the main reflector and sub-reflector respectively. These are included as

Table 2.1: The reflector specifications used for this study

D_m	15 m
β	57.6°
θ_e	58.0°
θ_0	-69.0°
L_s	2.69 m

they are used for estimating edge diffraction on the sub-reflector which is discussed later.

2.2.3 Feed Horn

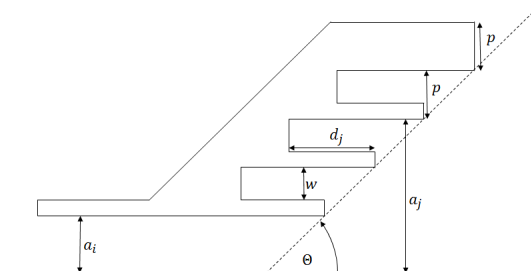


Figure 2.2: Original design diagram for axially corrugated horn. [1]

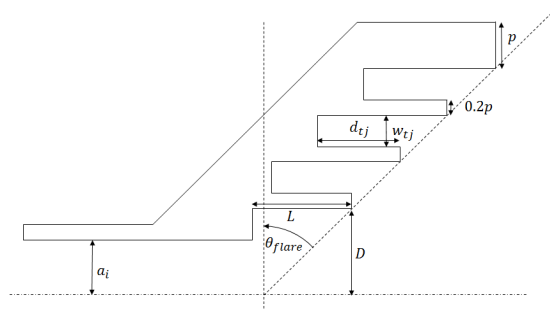


Figure 2.3: Modified axial corrugated horn design diagram

An axial choke horn was chosen for this design. Olver et. al. [9] showed that this type of feed functions well for low F/D ratio reflector systems. Additionally, the L-band feed designed by Lehmsiek and Theron [10] for MeerKAT was of this type. Finally Lehmsiek and de Villiers [5] also presented a horn of this type and showed that more than three chokes showed little improvement. As an initial base design the axial choke horn design found in “Modern Antenna Handbook” [1] was used and is shown in Figure 2.2. This design used maximum gain and wavelength as design parameters. The flare angle θ was fixed at 45° while the radius of the feed waveguide a_i , was calculated as

$$a_i = \frac{3\lambda}{2\pi}, \quad (2.1)$$

with free space wavelength at the centre frequency denoted as λ . The number of chokes N_{slots} was determined by

$$N_{slots} = \lfloor -343.325 + 84.7229G_{dBi} - 6.99153G_{dBi}^2 + 0.194452G_{dBi}^3 \rfloor, \quad (2.2)$$

with G_{dBi} representing the desired peak gain. Each choke was defined by three parameters two of which were constant across all the chokes. These were the width p , which included the width of the inner wall and the choke, calculated as

$$p = \frac{\lambda}{8}, \quad (2.3)$$

and the width of choke w , defined as

$$w = 0.8p. \quad (2.4)$$

It therefore follows that the radius to the outer wall of a given choke a_j would be

$$a_j = a_i + jp, j \in 1 \dots N_{slots}, \quad (2.5)$$

with j referring to the order of the chokes, counting away from the central axis. The third parameter was the depth of the choke d_j along the inner wall, as given by

$$d_j = \frac{\lambda}{4} \exp \left(\frac{1}{2.114 \left(\frac{2\pi a_j}{\lambda} \right)^{1.134}} \right), j \in 1 \dots N_{slots}. \quad (2.6)$$

In order to add more design flexibility, multiplicative factors were introduced to the depth and width of all the chokes

$$d_{tj} = d_j d_{fj}, j \in 1 \dots N_{slots}, \quad (2.7a)$$

$$w_{tj} = w w_{fj}, j \in 1 \dots N_{slots}. \quad (2.7b)$$

The factors d_{fj} and w_{fj} were real scalar constants applied to the depth and width respectively of a choke in position j . The new choke depth was denoted as d_{tj} and the new width was denoted as w_{tj} . A Visual Basic for Applications (VBA) script written to generate the model in *CST* [11] was designed to handle up to ten chokes all with

individual width and depth factors. This corresponded with the upper limit of G_{dBi} defined by the original design.

Additionally, the flare angle, redefined as θ_{flare} as shown in Figure 2.3, was allowed to vary and the radius of the feed waveguide was based on a desired TE_{11} mode cut-off frequency (f_c) derived from Balanis [12] as

$$a_i = \frac{1.8412}{2\pi f_c \sqrt{\mu_0 \epsilon_0}}, \quad (2.8)$$

with μ_0 and ϵ_0 defined as the permittivity and permeability of free space.

Finally a matching section was added so that feed waveguide radius could be kept constant while the radius of the horn's throat D , where the flare and the waveguide meet, could be altered. Both the throat radius, also referred to as step depth or taper depth, was defined as

$$D = a_i D_f, \quad (2.9)$$

with D_f referring to a real scalar factor. Likewise, the length of the matching section L is defined as

$$L = 2a_i L_f, \quad (2.10)$$

with L_f similarly defined as a real scalar factor. Keeping the radius of the feed waveguide constant was important to ensure that it would function in a single mode operation during optimisation.

The design parameters now consisted of f_c , θ_{flare} , and N_{slots} as well as the factors D_f , L_f , d_{fj} , and w_{fj} . This modified design, shown in Figure 2.3, was used throughout the study with some variations to the matching section. The frequency band of interest was 1 GHz to 1.5 GHz for all the investigations. Therefore, for all cases, the centre frequency was 1.25 GHz and f_c was chosen as 0.75 GHz in order to avoid TM_{11} mode propagation in the feed waveguide. Further, 11 frequency samples were used throughout this study.

Table A.1 in Appendix A shows the value for all the horn parameters with the multiplicative factors set to 1 that were used for all the investigations.

2.3 Sensitivity

Sensitivity is an important performance parameter when considering an antenna system for radio astronomy purposes. According to Kraus [13] this is because it is related to the minimum flux density that is detectable by an antenna system. Additionally, when incorporated into an interferometer, the sensitivity of the individual antenna elements is crucially important. From Wrobel and Walker [14] the reason for this is that, assuming a weak source, the minimum detectable flux density $F_{D,min}$ of an interferometer is

$$F_{D,min} = \frac{k_b}{S\eta_s \sqrt{N_{array}(N_{array} - 1)} f_{BW} t_{int}}, \quad (2.11)$$

with k_b referring to Boltzmann's constant (1.38×10^{-23} J K⁻¹). The system efficiency of the array elements is η_s and the number of array elements is N_{array} . The remaining two terms relate to the actual observation and are the observation bandwidth f_{BW} and the integration time t_{int} . Sensitivity is dependant on two antenna performance parameters through

$$S = \frac{A_e}{T_{sys}}. \quad (2.12)$$

These are the effective aperture area (A_e) and total system noise temperature (T_{sys}). These parameters relate to how much signal collecting area the system has and how noisy the system is respectively.

2.3.1 Effective Aperture

Balanis [12] defines the effective aperture area of an antenna as equal to the power received at the terminals of the antenna divided by the power density of an incident plane wave that is polarisation matched to the antenna. Alternatively, in equation form

$$A_e = \frac{P_t}{W_i}, \quad (2.13)$$

where P_t is the power at the antenna terminals and W_i is the power density of a plane wave incident on the antenna. In simpler terms this essentially refers to how "big" the antenna looks in a given direction. Equation (2.13) is not a particularly convenient way of computing the effective aperture area because the power density of an incident plane

wave needs to be know. A related parameter is aperture efficiency (η_t) which Balanis [12] defines as

$$\eta_t = \frac{A_e}{A_p}, \quad (2.14)$$

with A_p referring to the physical aperture area. This is simply the ratio of the effective aperture area to the physical aperture area. The effective aperture can therefore be calculated, by rearranging equation (2.14), from the aperture efficiency and the physical aperture area. Due to the highly collimated beam formed by parabolic reflector antennas the physical aperture is easy to define as the area of the projected aperture.

Aperture efficiency

Aperture efficiency is a useful means to calculate the effective aperture area are for several reasons. The first is that it is a proportional value and therefore easy to compare between systems. The second, for a parabolic reflector antenna, is that the aperture efficiency and peak directivity of the secondary pattern are proportional. Therefore the aperture efficiency can easily be derived from the secondary pattern through

$$\eta_t = \left(\frac{2\lambda}{\pi D_m} \right)^2 D_0, \quad (2.15)$$

with a peak secondary pattern directivity D_0 , and free space wavelength λ . The third reason is that there are long standing, accurate, and closed form approximations for the aperture efficiency of a parabolic reflector system given a known feed pattern. A particularly useful variant of this approximation was published by Kildal [15]. The usefulness of this interpretation was that it described aperture efficiencies in terms of body of revolution (BOR_n) mode coefficients.

The basis for this lies in the concept that the $\vec{\theta}$ and $\vec{\phi}$ components, $G_\theta(\theta, \phi)$ and $G_\phi(\theta, \phi)$, of a farfield radiation pattern $G(\theta, \phi)$ can be expanded into a Fourier series in ϕ . This Fourier series, of the form

$$G_\theta(\theta, \phi) = \sum_{n=0}^{\infty} (A_n(\theta) \sin(n\phi) + B_n(\theta) \cos(n\phi)), \quad (2.16a)$$

$$G_\phi(\theta, \phi) = \sum_{n=0}^{\infty} (C_n(\theta) \cos(n\phi) - D_n(\theta) \sin(n\phi)), \quad (2.16b)$$

constitutes the BOR_n modes and the terms $A_n(\theta)$, $B_n(\theta)$, $C_n(\theta)$, and $D_n(\theta)$ are the BOR_n coefficients as shown in Kildal and Sipus [16]. Furthermore, from Rusch and Potter [17], it had been shown that, for parabolic antennas, only the BOR_1 mode contributes to the radiation along boresight while the remaining modes constitute a power loss. Kildal [15] then rewrote the closed form approximation of aperture efficiency, now referred to as η_f , in terms of BOR_1 coefficients

$$\eta_f = 2 \cot^2 \left(\frac{\theta_e}{2} \right) \frac{\left| \int_0^{\theta_e} \text{CO}(\theta) \tan \left(\frac{\theta}{2} \right) d\theta \right|^2}{\int_0^\pi (|\text{CO}(\theta)|^2 + |\text{XP}(\theta)|^2) \sin(\theta) d\theta} \quad (2.17)$$

with the co-polar pattern $\text{CO}(\theta)$ and the cross-polar pattern $\text{XP}(\theta)$ of the feed pattern computed as

$$\text{CO}(\theta) = \frac{1}{2}(A_1(\theta) + C_1(\theta)), \quad (2.18a)$$

$$\text{XP}(\theta) = \frac{1}{2}(A_1(\theta) - C_1(\theta)), \quad (2.18b)$$

for a feed pattern, linearly polarized in the y -direction. The power lost in the other modes was then accounted for by adding a BOR_1 sub-efficiency (η_{BOR_1}). This meant that the total aperture efficiency η_t would be

$$\eta_t = \eta_{BOR_1} \eta_f. \quad (2.19)$$

What is particularly useful about this was that field integrations that formed part of the calculation of η_t , were now always one dimensional as opposed to two dimensional, significantly simplifying the calculation. Other approximations of η_t with single dimensional integrations have been proposed but had done so by assuming that the feed pattern was circularly symmetrical around the z axis with a main lobe along the z axis [18] [12]. Interestingly, this type of field pattern is in fact the BOR_1 mode. For fields not of this type, Yang et al [19] showed how the discrete Fourier transform of the primary farfield pattern could be used to calculate the BOR_n coefficients as

$$A_n(\theta) = \frac{2}{N_{cuts}} \sum_{k=0}^{N_{cuts}-1} G_\theta(\theta, k\Delta\phi) \sin(kn\Delta\phi), \quad (2.20a)$$

$$B_n(\theta) = \frac{2}{N_{cuts}} \sum_{k=0}^{N_{cuts}-1} G_\theta(\theta, k\Delta\phi) \cos(kn\Delta\phi), \quad (2.20b)$$

$$C_n(\theta) = \frac{2}{N_{cuts}} \sum_{k=0}^{N_{cuts}-1} G_\phi(\theta, k\Delta\phi) \cos(kn\Delta\phi), \quad (2.20c)$$

$$D_n(\theta) = \frac{2}{N_{cuts}} \sum_{k=0}^{N_{cuts}-1} G_\phi(\theta, k\Delta\phi) \sin(kn\Delta\phi), \quad (2.20d)$$

with the number of ϕ plane cuts used equal to N_{cuts} and $\Delta\phi$ equal to $2\pi/N_{cuts}$. With these n_f can be computed using equations (2.18) and (2.17) while η_{BOR_1} can be calculated by

$$\eta_{BOR_1} = \frac{\int_0^\pi (|A_1(\theta)|^2 + |B_1(\theta)|^2 + |C_1(\theta)|^2 + |D_1(\theta)|^2) \sin(\theta) d\theta}{\int_0^{2\pi} \int_0^\pi (|G_\theta(\theta, \phi)|^2 + |G_\phi(\theta, \phi)|^2) \sin(\theta) d\theta d\phi}. \quad (2.21)$$

An important note is that the denominator is simply the total radiated power and can be determined by using power normalization in *GRASP* [20]. Again this would avoid the need to calculate a two dimensional integral.

Another useful aspect of this approach is that if the feed pattern is linearly polarized and purely BOR_1 , or very close to it ($\eta_{BOR_1} \approx 1$), then it can be fully described either by the E-plane and H-plane patterns [15] or by the co-polar and cross-polar patterns in the $\phi = 45^\circ$ plane [16]. Therefore, measuring feed patterns of this type becomes considerably easier. Interestingly, if the feed pattern is circularly polarized, the co-polar and cross-polar patterns in the $\phi = 45^\circ$ plane still apply.

Kildal [15] further factorized η_f into a set of sub-efficiencies. These were the spillover efficiency (η_{sp}), the polarisation efficiency (η_{pol}), the illumination efficiency (η_{ill}), and the phase efficiency (η_{pha}) such that

$$\eta_f = \eta_{sp} \eta_{ill} \eta_{pol} \eta_{pha}. \quad (2.22)$$

Spillover efficiency essentially indicates how much power in the feed pattern is not intercepted by the reflectors and takes the form

$$\eta_{sp} = \frac{\int_0^{\theta_e} (|\text{CO}(\theta)|^2 + |\text{XP}(\theta)|^2) \sin(\theta) d\theta}{\int_0^{\pi} (|\text{CO}(\theta)|^2 + |\text{XP}(\theta)|^2) \sin(\theta) d\theta}. \quad (2.23)$$

The polarisation efficiency accounts for losses due to cross-polarisation and is calculated as

$$\eta_{pol} = \frac{\int_0^{\theta_e} |\text{CO}(\theta)|^2 \sin(\theta) d\theta}{\int_0^{\theta_e} (|\text{CO}(\theta)|^2 + |\text{XP}(\theta)|^2) \sin(\theta) d\theta}. \quad (2.24)$$

Illumination efficiency estimates to the uniformity with which the projected aperture is illuminated by the feed pattern as

$$\eta_{ill} = 2 \cot^2\left(\frac{\theta}{2}\right) \frac{\left(\int_0^{\theta_e} |\text{CO}(\theta)| \tan(\theta) d\theta\right)^2}{\int_0^{\theta_e} |\text{CO}(\theta)|^2 \sin(\theta) d\theta}. \quad (2.25)$$

The final sub-efficiency is phase efficiency which accounts for any phase errors in the projected aperture and is calculated as

$$\eta_{pha} = \frac{\left|\int_0^{\theta_e} |\text{CO}(\theta)| \tan(\theta) d\theta\right|^2}{\left(\int_0^{\theta_e} |\text{CO}(\theta)| \tan(\theta) d\theta\right)^2}. \quad (2.26)$$

These four sub-efficiencies can be an invaluable source of information when diagnosing poor performance of a particular feed pattern. Also, as aspects of aperture efficiency are often in opposition, such as η_{sp} and η_{ill} , these sub-efficiencies can help inform what sort of compromise is achieved with a given feed patten.

Finally a sixth sub-efficiency was included in the the form of a diffraction efficiency (η_{dif}). The diffraction efficiency accounts edge diffraction losses from the sub-reflector. Diffraction was not included in the formulation of equation (2.17) because, in general, the main reflector would be very large relative to the wavelength. For dual reflector systems, the sub-reflector can become small enough that edge diffraction starts to have a significant effect.

The diffraction efficiency approximation used was proposed by de Villiers [21]. This approximation is specifically for dual offset reflectors and took the form

$$\eta_{dif} = \left| 1 + \frac{n \sin^2 \left(\frac{\theta_e}{2} \right) \cos^n \left(\frac{\theta_e}{2} \right) (i-1) \Delta\rho}{1 - \cos^n \left(\frac{\theta_e}{2} \right) \sqrt{2\pi} D_m} \right|^2. \quad (2.27)$$

The term $\Delta\rho$ describes the transition region between the reflectors and is calculated as

$$\Delta\rho = \sqrt{\frac{\lambda(\rho_{m0} + \rho_{s0})}{\pi} \left| \frac{\rho_{m0}}{\rho_{s0}} \right|}, \quad (2.28)$$

with ρ_{m0} and ρ_{s0} referring to the distance from the prime focus to the centre of the main reflector and sub-reflector respectively as shown in Figure 2.1. The exponential n needs to be estimated by approximating the normalized feed gain pattern $D(\theta)$ with the form

$$D(\theta) = \cos^{2n} \left(\frac{\theta}{2} \right), \quad (2.29)$$

then setting $\theta = \theta_e$ and solving for n using the actual normalized feed pattern.

With the inclusion of η_{dif} the total aperture efficiency for a dual parabolic reflector system now becomes

$$\eta_t = \eta_{BOR_1} \eta_{sp} \eta_{pol} \eta_{ill} \eta_{pha} \eta_{dif}. \quad (2.30)$$

2.3.2 Total System Noise Temperature

Total system noise temperature is essentially a measure of the influence of various sources environmental noise on an antenna system. This parameter is commonly broken

into two constituent parts by

$$T_{sys} = T_{ant} + T_{rec}, \quad (2.31)$$

with the antenna noise temperature T_{ant} and the receiver noise temperature T_{rec} . The receiver noise temperature is the result of noise and losses in the electronics as well as the physical temperature of the feed antenna. For the purposes of calculation this is generally estimated; for this study a $T_{rec} = 15$ K was used.

The antenna noise temperature is the result of environmental sources of noise such as background radiation, atmospheric radiation, ground scattering and ground emission.

According to de Villiers and Lehmensiek [22], T_{ant} is computed, with the antenna pointing in a particular direction \vec{r}_0 , using the radiated power-normalized noise integral

$$T_{ant,r_0} = \frac{\int_0^{2\pi} \int_0^\pi N_{\vec{r}_0}(\theta, \phi) \sin(\theta) d\theta d\phi}{\int_0^{2\pi} \int_0^\pi G(\theta, \phi) \sin(\theta) d\theta d\phi}, \quad (2.32)$$

again with the secondary radiation pattern $G(\theta, \phi)$ and

$$N_{\vec{r}_0}(\theta, \phi) = T_b(\theta, \phi)G_{\vec{r}_0}(\theta, \phi). \quad (2.33)$$

The function $T_b(\theta, \phi)$ is the brightness distribution seen when viewed from the antenna and $G_{\vec{r}_0}(\theta, \phi)$ is the secondary radiation pattern pointing in the direction \vec{r}_0 . There are several models of varying complexity that can be used for $T_b(\theta, \phi)$ and an overview of these are given by de Villiers and Lehmensiek [22]. For the purposes of this study *Model 3* was used which contained most of the complexity, foregoing only the polarisation

dependence of *Model 4* which was the most complete model.

An approximate technique that reduced the computational cost of this calculation was proposed by Imbriale [23]. The essence of this technique lay in using only the primary pattern and the sub reflector for the noise integral rather than the full secondary pattern. This could be done by applying a mask over the region of T_b that contained the main reflector. This mask contained the temperature of the sky in the direction that the main reflector was pointing in. A correction factor α was included to account for a minor back lobe formed by the reflected field of the main reflector. This minor back lobe was due to diffraction effects on the edge of the main reflector.

2.4 Side Lobe Level

Side lobe level (SLL) is an important consideration for any antenna and particularly so for those destined for radio astronomy. This is because the presence of side lobes in the secondary pattern causes distortions and artefacts during the imaging process [13]. The higher the SLL, the more prominent these distortions and artefacts become. Therefore the SLL is an important performance parameter to consider.

The difficulty with the measurement of SLL is the definition of what constitutes a side lobe. The simplest definition would be to look for local peaks in the pattern other than the main lobe. The problem with this is that patterns with particularly wide main lobes can partially obscure some of the side lobes. This can then leave a shoulder on the main lobe that effects the pattern performance similarly to a true side lobe. If this is not included the SLL could be under estimated as well as become very noisy over frequency or design parameters. The reason for this is that the SLL will tend to jump as a side lobe begins to be subsumed by the main lobe.

Including these shoulders as part of the definition means that local peaks alone are no longer a viable means of determining SLL. Another problem is that, with no real local maximum, the level of these shoulders are ambiguous. An option is to use the saddle created by a shoulder and use this as the associated SLL. This could be done by looking for where the second derivative goes to zero, otherwise known as an inflection point which would then become the first SLL.

Chapter 3

Space Mapping

3.1 Introduction

The first surrogate modelling technique investigated was space mapping. A brief explanation of the technique will be given and how it could be used as part of a single-objective optimisation. The techniques applied to the modelling of aperture efficiency and its potential use will be discussed.

3.2 Fundamental Concept

Space mapping (SM) refers to a process of creating a map from the response of a coarse model $R_c(x)$ to that of a corresponding fine model $R_f(x)$. The map takes the form of multiplicative and additive factors that are applied to aspects of the coarse model. The resulting response of the augmented coarse model, or surrogate model, $R_{s,i}(x, p)$ would then be in closer alignment with that of the fine model.

When applied to SOO, this means that a computationally inexpensive coarse model could be used with greater accuracy resulting in a reduction in computational cost while maintaining accuracy similar that of the fine model. The use of the SM in an optimisation does require additional iterations of surrogate alignment and optimisation because the surrogate needs to be realigned each time the optimisation finds a new optimum away from the last point of alignment. The assumption is that the coarse model would be sufficiently fast, relative to the fine model, that there is still an overall reduction in computation time.

SM is described in general terms as

$$R_f(x) \approx R_{s,i}(x, p_i), \quad (3.1)$$

with x referring to a vector of dimensions $N \times 1$ of input values for corresponding design variables and p_i referring to the SM parameters that control the mapping. An important point underpinning SM is the assumption that the coarse model behaves similarly to the fine model. This is not to say that an alignment cannot be achieved at a given point if this is not the case. Rather any alignment would become invalid far quicker when moving away from that point making the alignment less useful. To date many types of SM have been developed to deal with a variety of optimisation problems. For this thesis only Traditional or Input SM (TSM), Output SM (OSM), and Implicit SM (ISM) are considered. This is because these cater to a variety of problems with little additional complexity. General implicit SM (GISM) combines all three and is the form that was used for this study.

3.2.1 Input SM

TSM modifies the model inputs to align the coarse response with the fine response. This is done through a multiplicative input parameter B and an additive parameter c in the form

$$R_{s,i}(x, p) = R_c(Bx + c). \quad (3.2)$$

The responses R_s and R_c are vectors of dimensions $M \times 1$ representing M responses. The multiplicative parameter B takes the form of a matrix of dimensions $N \times N$ while the additive parameter c is a vector of dimensions $N \times 1$.

3.2.2 Output SM

As opposed to TSM, OSM directly modifies the response of the coarse model. The OSM parameters are A for the multiplicative case and d for the additive case and are applied as

$$R_s(x, p) = AR_c(x) + d. \quad (3.3)$$

The multiplicative factor A is a diagonal matrix with dimensions $M \times M$ and the additive parameter d is a vector of dimensions $M \times 1$. A useful aspect of OSM is that d enforces perfect zero order alignment between $R_s(x, p)$ and $R_f(x)$. This can be seen in the parameter extraction in equation (3.7). It must be noted that the zero order alignment is only perfect for x where the alignment was performed.

3.2.3 Implicit SM

ISM modifies constants that are internal to the coarse model. This differs from TSM and OSM because the parameter being modified is not an input parameter of the model and takes the form

$$R_s(x, p) = R_c(x, Gx + x_p). \quad (3.4)$$

The modification of the internal constants are dependant on the input variables. This means that for Q internal constants, G is a $Q \times N$ matrix and x_p is a vector of size $Q \times 1$.

3.2.4 Generalized Implicit Space Mapping

Koziel et al [24] proposed a generalized SM algorithm that combined TSM, OSM, and ISM called Generalized implicit SM (GISM). A simplified version

$$R_s(x, p) = AR_c(Bx + c, Gx + x_p) + d, \quad (3.5)$$

was used with the SM parameters being identical to those above. The majority of the SM parameters, excluding d , are computed according to

$$(A, B, c, G, x_p) = \underset{(A, B, c, G, x_p)}{\operatorname{argmin}} \varepsilon(A, B, c, G, x_p), \quad (3.6a)$$

$$\varepsilon(A, B, c, G, x_p) = \|R_f(x) - AR_c(Bx + c, Gx + x_p)\|. \quad (3.6b)$$

An important note is that the alignment only requires additional coarse evaluations as $R_f(x)$ has no direct interaction with the SM parameters. Once these parameter have been computed, the OSM additive term d equals any remaining residuals

$$d = R_f(x) - AR_c(Bx + c, Gx + x_p). \quad (3.7)$$

The flexibility in the GISM approach is that SM parameters can still be chosen to tailor the model to a specific problem. Parameters can be removed from the model by locking the parameters to values of one for the diagonals of A and B , or zero for c , d , and the off-diagonal values of A and B . This is quite important because the choice of SM parameter can usually be linked to a physical aspect of the problem. A good choice partially compensates for the errors in the coarse model and so the surrogate will lose accuracy slower as one moves away from the point of alignment. A poor choice may be completely unable to align, assuming d is not included, the models or if an alignment is possible it is likely to be very narrow and possibly misleading.

3.2.5 Single-Objective optimisation using SM

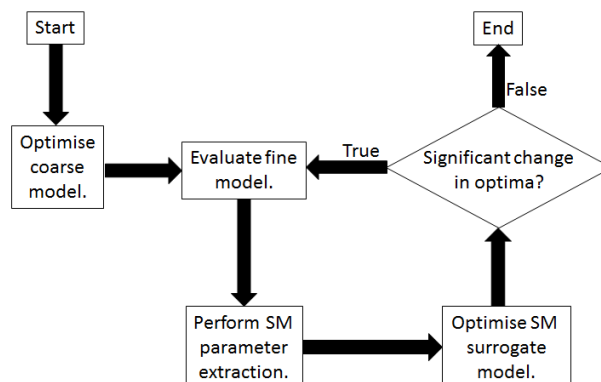


Figure 3.1: High level diagram of SM optimisation cycle.

Applying SM to SOO is done by repeated iterations of surrogate alignment and optimisation as shown in Figure 3.1. As long as the coarse model at the core of the surrogate shows similar trends to the fine model, each successive iteration should see the optimum of the surrogate move closer to the optimum of the fine model. This also assumes that the appropriate SM parameters have been chosen. Between iterations the optima of the surrogates are compared for significant change to determine if further iterations are necessary.

An important note is that this technique requires multiple optimisation runs. In fact each iteration likely requires at least two optimisations to be performed: one during the SM parameter extraction and then the actual optimisation on the surrogate. It is therefore important that the coarse model be significantly faster than the fine model. As

fine models are frequently full wave simulations and coarse models are often closed form approximations or equivalent circuit models this is regularly the case. Again a suitable choice of SM parameters is important because the better the surrogate retains accuracy away from the point of alignment, the fewer iterations are required before the optimum is found.

3.3 Application to Reflector Feed Design

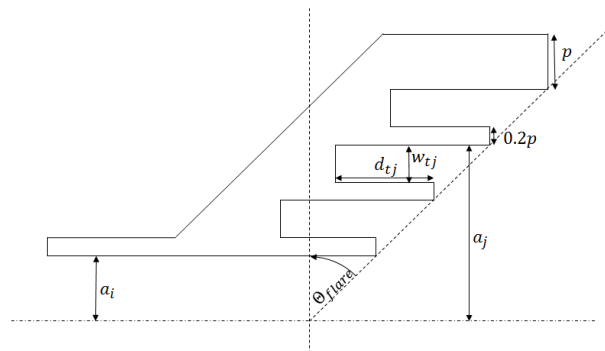


Figure 3.2: The horn profile used for the SM investigation with three chokes and no matching section.

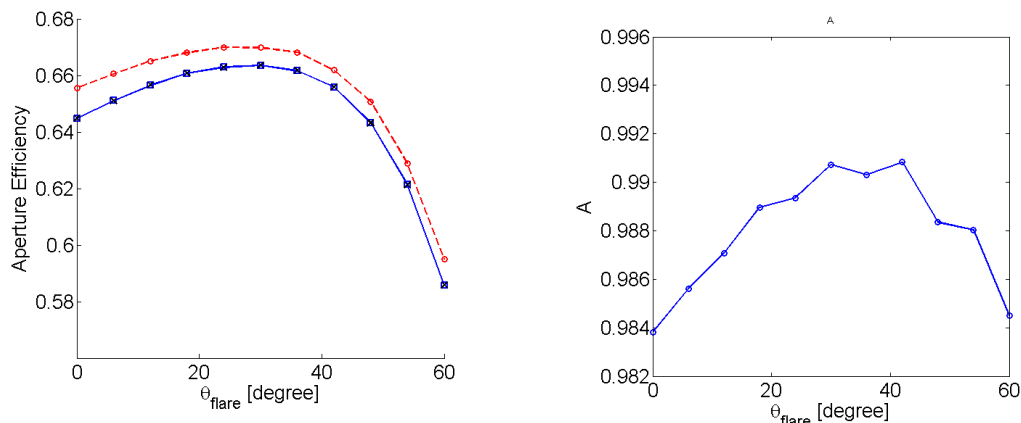
The potential use of SM based optimisation applied to the aperture efficiency of the feed horn in Figure 3.2 was investigated. For the coarse model, a coarsely meshed *CST* simulation of the horn was used to generate the feed pattern. A MATLAB [25] script was then used to extract the farfield pattern and apply the closed form approximation discussed in Section 2.3.1. The fine model used a dense mesh for the *CST* simulation and the farfield was then extracted and used as the feed pattern for a *GRASP* [20] simulation of the full reflector system. The peak directivity of the secondary pattern was then extracted and used to calculate the aperture efficiency as discussed in Section 2.3.1.

3.3.1 Experimental Design

A fairly simple experiment was run to assess the suitability of some of the SM parameters for use in an SOO. The experiment consisted of sweeping 11 points along a design parameter while generating $R_f(x)$, $R_s(x, p)$, and $R_c(x)$ as well as recording the value of the SM parameter at each point. This was done separately for two SM parameters, namely A and c . For simplicity only the flare angle was used as the design parameter with no matching section and each evaluation was performed with a single frequency sample at 1.4 GHz. The expectation was that a well matched SM parameter

would show a smooth flat response while a poorly matched one would show a large range of values with a high rate of change and possibly discontinuities.

3.3.2 Results



(a) Response over θ_{flare} for R_f (blue solid line), R_c (red dashed line), and R_s (black crosses).

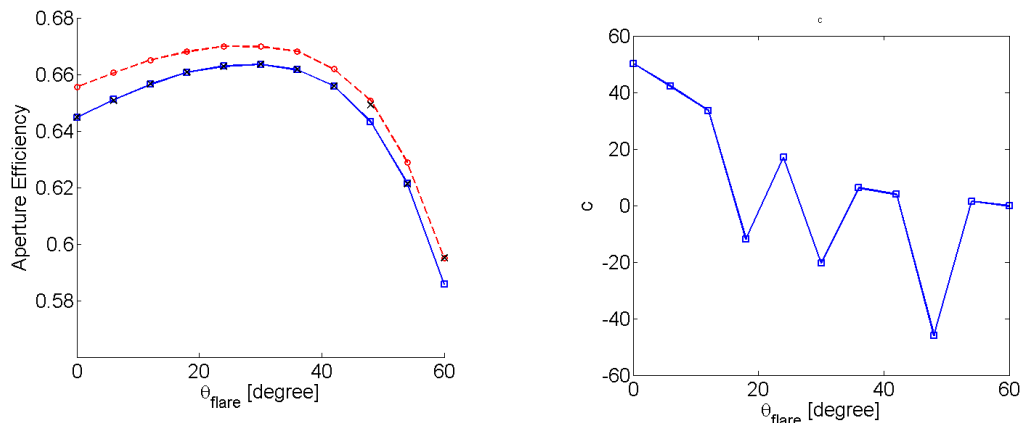
(b) The value of the SM parameter A used by R_s over θ_{flare} .

Figure 3.3: These figures show the results of the experiment while using SM parameter A . The responses over flare angle are shown in (a) with R_f (blue solid line), R_c (red dashed line), and R_s (black crosses) while the value of the SM parameter A used for R_s at each point is shown in (b).

Figure 3.3 shows the result of the sweep when using the multiplicative OSM parameter A . The fine and coarse response curves are seen as blue and red lines respectively in Figure 3.3a which shows a consistent overestimation by the coarse model. Looking at the values of A over θ_{flare} in Figure 3.3b shows that there is little variation in A over the whole range of θ_{flare} . It is clear then that using a surrogate with A would work well for optimisation.

This could be expected as the majority of the error remaining in the closed form approximation of aperture efficiency was due to diffraction effects that had not been fully accounted for by the closed form approximation. As seen in Section 2.3.1, diffraction effects can be modelled as another sub-efficiency due to the fact that it represents power loss with respect to the aperture field. This also means that the performance of the surrogate would likely be maintained as more design parameters are included.

The results of the sweep using A contrasted starkly with those using the additive ISM parameter c shown in Figure 3.4. The range of values that c assumed was almost as large as the range of θ_{flare} , in absolute terms, which indicates that the surrogate had trouble staying aligned using c . Additionally, Figure 3.4b shows that c took on both



(a) Response over θ_{flare} for R_f (blue solid line), R_c (red dashed line), and R_s (black crosses).

(b) The value of the SM parameter c used by R_s over θ_{flare} .

Figure 3.4: These figures show the results of the experiment while using SM parameter c . The responses over flare angle are shown in (a) with R_f (blue solid line), R_c (red dashed line), and R_s (black crosses) while the value of the SM parameter c used for R_s at each point is shown in (b).

negative and positive values. This could be explained by the response curves in Figure 3.4a. The effect of c on the response curve, at least when using one design parameter, is to shift the whole curve either left or right. The peak in the response curve near $\theta_{flare} = 30^\circ$ means there are in general two values of c that will produce an alignment. The misaligned surrogate responses seen in Figure 3.4a are, in part, due to this as the optimisation during parameter extraction may find a distant local optima and cannot actually align the models.

When looking at the response curves, it can be seen that the position of the peak with respect to θ_{flare} was largely aligned for both R_f and R_c . Therefore any shift of the response curve along θ_{flare} could actually be considered a misalignment.

3.3.3 Challenge of Applying SM

The experiment highlighted a larger problem when applying SM to the optimisation of a feed horn for a dual reflector system. The problem was that the coarse model was too slow relative to the fine model to deliver improved performance because the coarse model still required the primary pattern. With no means to approximate the primary pattern in any meaningful way without the use of a full wave simulation, the coarse model had to use a *CST* simulation to generate the primary pattern. Attempts were made to improve the speed of the coarse *CST* simulation by reducing the mesh density significantly the improvement was marginal. Even when considering the likely increase in computational time of the *GRASP* simulation with higher frequency bands and more

frequency samples, the difference was not going to be of the order of magnitude needed for SM optimisation to offer significant improved performance.

Therefore unless the simulation in the coarse model can be replaced with some significantly faster approximation SM based optimisation is not really viable for the optimisation of dual reflector feeds. For this reason SM was abandoned for the purposes of this study.

Chapter 4

Multi-objective optimisation

4.1 Introduction

For the investigation to follow a multi-objective optimizer was implemented. The basic concepts of optimisation in general will be discussed as well as concepts specific to multi-objective optimisation MOO. The MOPBIL algorithm will be discussed and its implementation described. Finally a set of testing functions will be detailed and the results of testing the implementation reported.

4.2 Fundamental Concept

In the broadest terms, optimisation looks to find the "*best*" solution to a given problem. Zitzler et al [26] define the problem generally as an objective function, sometimes called a fitness function or cost function, $f(x)$. The input x of the objective function is referred to as a solution and falls within the solution space X which contains all possible valid inputs of $f(x)$. The fitness of a given solution x is the value of $f(x)$ and is denoted as y which falls within the objective space Y that contains all possible outputs of $f(x)$

$$y = f(x), \quad x \in X \quad y \in Y. \quad (4.1)$$

For the SOO case Y is a one dimensional space. For a minimization, there exists a solution $x_1 \in X$ such that $f(x_1) < f(x_2)$ for all possible $x_2 \in X$. An interesting observation is that if $Y \in \mathfrak{R}$ with $y_1 = f(x_1)$ and $y_1 \in Y$, y_1 is a point that forms a boundary between Y and lower values in the \mathfrak{R} space.

4.2.1 Single- vs. Multi-objective optimisation

For the MOO case Y is a two or more dimensional space. This means that, in general, there is no longer a single solution x_1 such that $f(x_1) < f(x_2)$ for all possible x_2 . So the concept of Pareto dominance was introduced [26]. If two points in the objective space, namely y_1 and y_2 , are considered then the requirement for y_1 to dominate y_2 ($y_1 \succ y_2$) is

$$\begin{aligned}
 Y &\in \mathfrak{R}^n, \\
 y_1, y_2 &\in Y, \\
 y_1 &= [y_{1_1}, \dots, y_{1_n}], \\
 y_2 &= [y_{2_1}, \dots, y_{2_n}], \\
 i &= 1 \dots n, \\
 y_1 \succ y_2 &\Leftrightarrow y_{1_i} \leq y_{2_i} \forall i \wedge y_{1_i} < y_{2_i} \exists i.
 \end{aligned} \tag{4.2}$$

What this means is that all the elements of y_1 must be less than or equal to the corresponding elements of y_2 . At the same time, at least one element of y_1 must be strictly less than the corresponding element of y_2 . Therefore moving from y_2 to y_1 improves the fitness in at least one dimension without deteriorating any of the others. Consider the example in Figure 4.1. The point y_1 is an improvement over point y_2 along both axes D_1 and D_2 therefore, y_1 dominates y_2 . Alternatively, y_1 improves on y_3 along the D_1 axis while y_3 improves on y_1 along the axis D_2 . This then means that y_1 does not dominate y_3 and visa versa. Finally the number of points that a point is dominated by is referred to as its dominance rank. Non-dominated solutions are therefore rank 0.

Additionally, if $y_1 \succ y_2$, then x_1 is said to also dominate x_2 even though the criterion for domination is entirely based within the objective space. Using Pareto dominance it is possible now to find a set of points in Y that are not dominated by any other points. These points are termed the Pareto front while the associated solutions in X are termed the Pareto set. The Pareto set represents a set of solutions that can only ever be improved in one dimension at the cost of another. Returning to the idea of optima as a boundary, the Pareto front will now form a boundary of one lower dimensions than the space in which it exists. For example, a line forms a boundary in a two dimensional space. Extending this to an N-dimensional space, the boundary then becomes a hyperplane in the N-dimensional space.

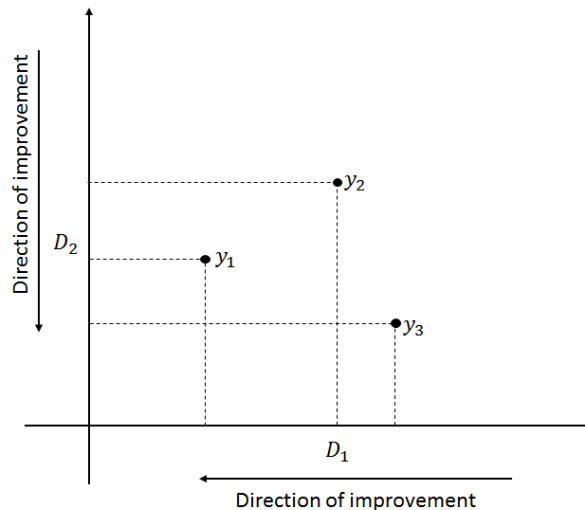


Figure 4.1: Diagram of a two dimensional space with three example points y_1 , y_2 , and y_3 . The additional arrows next to the axes show the direction of improvement for the purposes of Pareto dominance.

4.2.2 Important Features of a MOO

There are a plethora of MOO algorithms drawing on a variety of techniques to generate the global Pareto set. Deb [27] asserts that the most important aspects for any MOO algorithm are that it moves toward the global Pareto front while adequately exploring the solution space. These are, by definition, conflicting processes as one promotes specialization while the other promotes generalization. For the purpose of this thesis the discussion of MOO algorithm will be kept to multi-objective evolutionary algorithms (MOEA) and specifically the MOPBIL algorithm that was used. MOEAs are a group of algorithms that use a fitness criterion on a population of solutions to choose the best solutions. These solutions are then used in the creation of the next population.

Exploring the space

The capability of a MOEA to explore a solution space essentially refers to the diversity in the population. A capacity for exploration is important for two reasons. The first is to ensure that the solution space is adequately searched. In general, MOEAs are non-exhaustive by design because they aim to reduce the computational cost. This means that a MOEA has a probability of mistaking a local Pareto front for the global Pareto front, which is negatively correlated to the degree that it searches the solution space. The second reason is to ensure that the whole Pareto front is filled. Again if the population lacks diversity the MOEA might only populate sections of the Pareto front leading to an artificially non-contiguous result.

Moving toward the Pareto Front

The purpose of any MOEA is to approximate the global Pareto front as closely as possible. This requires the population to be specialized in order to improved the likelihood that a solution in, or near to, the global Pareto set is produced at each generation. The first issue is that some sort of specialization needs to happen. The obvious threat to this is a defective algorithm. A more plausible and difficult threat are featureless regions in the objective space that could give no information to the MOEA. A second issues is that the population could be specialized on the wrong region of the objective space. These regions are generally formed by local Pareto fronts and can stall the progress of a MOEA towards the global Pareto front.

4.3 Implementation

The MOPBIL implementation described by Bureerat and Sriwornamas [28] was used. This implementation is very similar to a basic PBIL implementation but with the inclusion of an archived elitism mechanism.

4.3.1 PBIL

PBIL was first proposed by Baluja [29]. It employs a probability vector to generate a population at each iteration of the optimisation. The populations consist of a set of binary strings that each represent a solution. The population is then evaluated by the objective function and the probability vector is trained toward the best solution according to

$$P_{new} = P_{old}(1 - l_r) + b l_r, \quad (4.3)$$

with P_{new} and P_{old} as the next and current probability vectors with elements ranging between 1 and 0. The term l_r is the learning rate of the algorithm and should be specified between 1 and 0 and b is the best solution vector from the previous population that is automatically included in the next generation. The principle is that as the optimisation iterates, the elements of the probability vector tend towards either 1 or 0 depending what the trend in best solutions indicate. The individual elements will experience differing rates of variance through iterations but in general the probability vector should start to partially mimic the global optimum and so increase the probability of a population containing the global optimum.

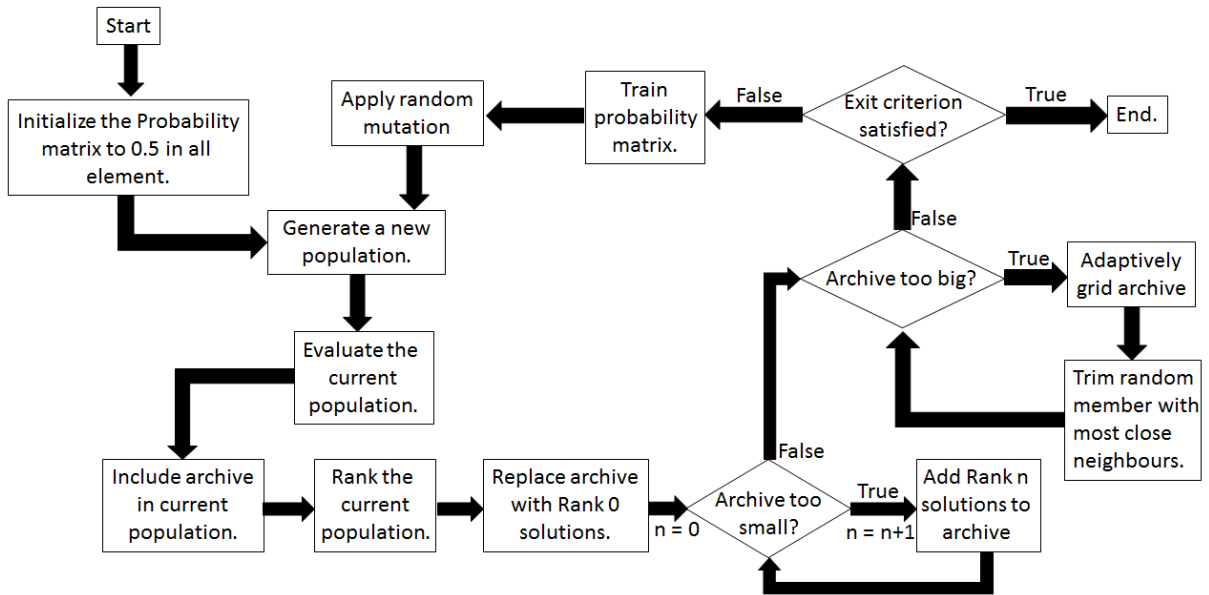


Figure 4.2: High level diagram of the MOPBIL implementation.

After training a mutation can then be applied to the probability vector. The mutation improves the exploration of the solution space as well as guards against training onto a local optima and is described by

$$P_{new} = P_{old} (1 - m_s) u(m_p) + m_s u(0.5) u(m_p). \quad (4.4)$$

Here m_s is the mutation shift while $u(x)$ is a function that randomly generates a binary string where the probability of a specific bit being a one is x . Therefore, m_p is the probability that a mutation will be applied to given probability vector element while the $u(0.5)$ term dictates if it is shifted toward zero or one.

Exiting the algorithm can be based on a few criterion. The algorithm can be run for a given number of iterations or solution evaluations. A particularly useful criterion is maximum number of iterations with no change in the best solution as stability in the best solution over several generations would indicate that the probability matrix is largely converged.

4.3.2 MOPBIL

A high level diagram of a MOPBIL implementation is shown in Figure 4.2. In order to maintain diversity in the population MOPBIL uses a probability matrix, as opposed to a single probability vector, that is made up of l probability vectors. This means that each probability vector generates N/l members of the population where N is the population

size. Additionally, instead of a single best solution being retained between iterations, an archive of non-dominated solutions is retained. After the population is generated and evaluated the current population and archive are combined and the solutions are evaluated for Pareto dominance. The non-dominated solutions are retained and replace the current archive. MOPBIL uses the same learning algorithm as shown in equation (4.3) but applies it to each probability vector independently by generating a different b vector for each probability vector. This is done by changing b to a vector that is averaged over a random set of n solutions from the archive. This is done in order to maintain variation in the probability matrix and therefore in the population.

Where the number of non-dominated solutions exceed the stipulated maximum archive size, an adaptive grid algorithm is used to randomly remove solutions from the most densely populated regions of the objective space. The algorithm works by dividing the objective space 2^g times along each of the N dimensions. This allows for each solution to be assigned a $N \cdot g$ bit binary grid reference. Solutions can then be removed from the most densely populated grid reference first. This would then improve the overall distribution of the Pareto front.

4.3.3 Unique to the Implementation

A persistent issue encountered that was not addressed by Bureerat and Sriworamas [28] was a tendency for overspecialisation of the probability matrix when the archive became too small. This invariably happened where a few solutions were generated within a generation that dominated the entire population and archive. The archive would then contain only a few solutions that the probability matrix would train onto. This would lead to a homogeneous probability matrix that had no capability to explore the solution space any further.

An initial solution was to impose a minimum size limit on the archive. If the archive fell below this limit it was emptied. This meant that the probability matrix could not train on a small solution set and overspecialise. Also, as the probability matrix was untouched, no training progress was lost. This helped reduce the tendency to overspecialise but still could not completely prevent it. This was because often the probability matrix had already partially overspecialised.

A better solution was to temporarily improve the solution space exploration. This was done by again imposing a minimum size on the archive. If the archive fell below this limit the non-dominance condition was relaxed by including solutions from the current population of increasing dominance rank until the archive size was above the limit.

The trimming of the archive was also handled slightly differently. There was a worry

that if a very fine adaptive grid was used the number of solutions with the same grid reference could tend to zero. At this point the trimming becomes entirely random and no longer explicitly promotes an even distribution along the Pareto front. To prevent this, the grid reference was used to calculate the distance between archive members in terms of grid blocks. Then if the archive was too large, archive members would be randomly removed starting with those that had a zero distance to another archive member. For a coarse adaptive grid with a large archive this functioned identically to the method used in [28] while for smaller archives with very fine adaptive grids it would continue to promote even distribution along the Pareto front.

A major drawback is that this greatly increases the computational cost of the adaptive grid process which was one of the major benefits it provided. In practice though this has not been noticed during testing as the population evaluation and dominance ranking uses far more computation time.

Finally, Gray encoding was included for the function wrapper. This was done to avoid issues like hamming cliffs where the binary representation of some adjacent numbers differs in every bit position. The wrapper simply converted from the binary, or Gray code, to a vector of decimal inputs for the objective function.

4.4 Testing the Implementation

The test functions presented by Zitzler et al [30] were used to test this MOPBIL implementation. The six test functions are aimed at testing a MOEA's ability to cope with different challenges. These relate to the shape of the global Pareto front, the effect of different local Pareto fronts, and the distribution of the objective space. The MOPBIL implementation was only compared to a random search with elitism as the optimiser was not the main focus of this study.

4.4.1 The test functions

The six functions defined by Zitzler et al [30] are named \mathcal{T}_1 to \mathcal{T}_6 . All six had a two dimensional objective space and an n dimensional solution space. Internally all the test functions have the same structure, consisting of a set of functions that are used to generate the response vector. This general structure of the test functions is shown as

$$\begin{aligned}
\mathbf{x} &= [x_1, \dots, x_n], \\
\mathcal{T}_i(\mathbf{x}) &= (f_1(x_1), f_2(\mathbf{x})), \\
f_2(\mathbf{x}) &= g(x_2 \dots x_n)h(f_1, g(x_2 \dots x_n)).
\end{aligned} \tag{4.5}$$

The functions $f_1(x_1)$, $h(f_1, g)$, and $g(x_2 \dots x_n)$ are defined individually by each test function. Each test function was devised so that the global Pareto front would be returned when the function g was set to some constant value. Having this known was ideal for testing because an objective measure could be taken of how close a given optimisation approximated the global Pareto front. Another particularly useful attribute of this structure was that the shape of the Pareto front could be defined through $h(f_1, g)$ while the distribution of the objective space could be defined through $g(x_2 \dots x_n)$.

With this general structure defined, the individual test functions are detailed below and were taken directly from Zitzler et al [30]. These were originally based on challenges to MOEAs presented by Deb [27] who divided them into two broad groups. These were challenges to exploration and challenges to convergence towards the global Pareto front.

The ability of an MOEA to explore the solution space refers to the diversity of the population and how it was maintained through the iterations. Challenges to this came from the curvature of the the Pareto front (\mathcal{T}_1 and \mathcal{T}_2), a non-continuous Pareto front (\mathcal{T}_3), and non-uniformity of the objective space (\mathcal{T}_6). Convergence towards the Pareto front refers to an increased likelihood of a population containing members on the global Pareto front. The highlighted challenges to this were multi-modality in the objective space (\mathcal{T}_4) and a deceptive front (\mathcal{T}_5).

\mathcal{T}_1 : Convex Pareto front

The function \mathcal{T}_1 presented a convex global Pareto front relative to the minimum in all dimensions. The specific potential challenge presented by a convex Pareto front was that the points positioned toward the centre of the front dominate a larger region than those positioned toward the edges. This could create a bias towards the central region of the Pareto front in some MOEA implementations. The internal functions of \mathcal{T}_1 were defined

as

$$\begin{aligned}
f_1(x_1) &= x_1, \\
g(x_2 \dots x_n) &= 1 + 9 \frac{\sum_{i=2}^n x_i}{n-1}, \\
h(f_1, g) &= 1 - \sqrt{\frac{f_1}{g}},
\end{aligned} \tag{4.6}$$

with $n = 30$, $x_i \in [0, 1]$, and the global Pareto front was formed at $g(x_2 \dots x_n) = 1$.

\mathcal{T}_2 : Concave Pareto front

Related to \mathcal{T}_1 , the function \mathcal{T}_2 presented a concave global Pareto front defined similarly to \mathcal{T}_1 . The challenge presented was also similar to that of \mathcal{T}_1 but with the bias being towards the edges rather than the central region of the Pareto front. The constituent functions were defined as

$$\begin{aligned}
f_1(x_1) &= x_1, \\
g(x_2 \dots x_n) &= 1 + 9 \frac{\sum_{i=2}^n x_i}{n-1}, \\
h(f_1, g) &= 1 - \left(\frac{f_1}{g}\right)^2,
\end{aligned} \tag{4.7}$$

with $n = 30$, $x_i \in [0, 1]$, and the global Pareto front was formed at $g(x_2 \dots x_n) = 1$.

\mathcal{T}_3 : Non-continuous Pareto front

A non-continuous global Pareto front was presented by \mathcal{T}_3 . This meant that a set of discrete sub-regions existed along the Pareto front. The challenge here was that the points in certain subregions could be removed prematurely. This would have precluded that section of the Pareto front from being filled. To this end the internal functions were defined as

$$\begin{aligned}
f_1(x_1) &= x_1, \\
g(x_2 \dots x_n) &= 1 + 9 \frac{\sum_{i=2}^n x_i}{n-1}, \\
h(f_1, g) &= 1 - \sqrt{\frac{f_1}{g}} - \left(\frac{f_1}{g}\right) \sin(10\pi f_1),
\end{aligned} \tag{4.8}$$

with $n = 30$, $x_i \in [0, 1]$, and the global Pareto front was formed at $g(x_2 \dots x_n) = 1$. An important note is that, due to the sin function in h , the Pareto front was discontinuous but the solution space was not.

\mathcal{T}_4 : Objective space multi-modality

Test function \mathcal{T}_4 presented a multi-modal objective space with 21^9 local Pareto fronts. The challenge here was that each local Pareto front could potentially stop a MOEA from continuing to converge on the global Pareto front. To generate these local fronts the internal functions took the form

$$\begin{aligned} f_1(x_1) &= x_1, \\ g(x_2 \dots x_n) &= 1 + 10(n-1) + \sum_{i=2}^n (x_i^2 - 10 \cos(4\pi x_i)), \\ h(f_1, g) &= 1 - \sqrt{\frac{f_1}{g}}, \end{aligned} \tag{4.9}$$

with $n = 10$, $x_1 \in [0, 1]$, $x_2 \dots x_n \in [-5, 5]$, and the global Pareto front at $g(x_2 \dots x_n) = 1$. Additionally the best local Pareto front was at $g(x_2 \dots x_n) = 1.25$.

\mathcal{T}_5 : Deceptive Pareto front

A deceptive local Pareto front is presented by \mathcal{T}_5 . The challenge differed from the multi-modal case in the fact that the deceptive Pareto front was favoured by the objective space over the global Pareto front. Additionally, \mathcal{T}_5 differed in construction from the other test functions in that the input was a set of binary strings that are processed by unitation function u and the piecewise function v as follows

$$\begin{aligned} f_1(x_1) &= 1 + u(x_1), \\ g(x_2 \dots x_n) &= \sum_{i=2}^n v(u(x_i)), \\ h(f_1, g) &= \frac{1}{f_1}, \\ v(u(x_i)) &= \begin{cases} 2 + u(x_1) & \text{if } u(x_i) < 5 \\ 1 & \text{if } u(x_i) = 5 \end{cases}, \end{aligned} \tag{4.10}$$

with $n = 11$, $x_1 \in \{0, 1\}^{30}$, $x_2 \dots x_n \in \{0, 1\}^5$, and the global Pareto front at $g(x_2 \dots x_n)$.

The deceptive Pareto front was formed at $g(x_2 \dots x_n) = 11$.

\mathcal{T}_6 : Non-uniform objective space

The test function \mathcal{T}_6 presented an objective space with a non-uniform distribution. The non-uniformity had been tailored to present two distinct problems. The first was that global Pareto front has a higher density towards the region where $f(x_1) = 1$. The second was that the density of the objective space was lowest near the global Pareto front. This meant that not only was there a statistical bias away from the global Pareto front but also away from certain regions of the front more so than others. To achieve this the internal functions were

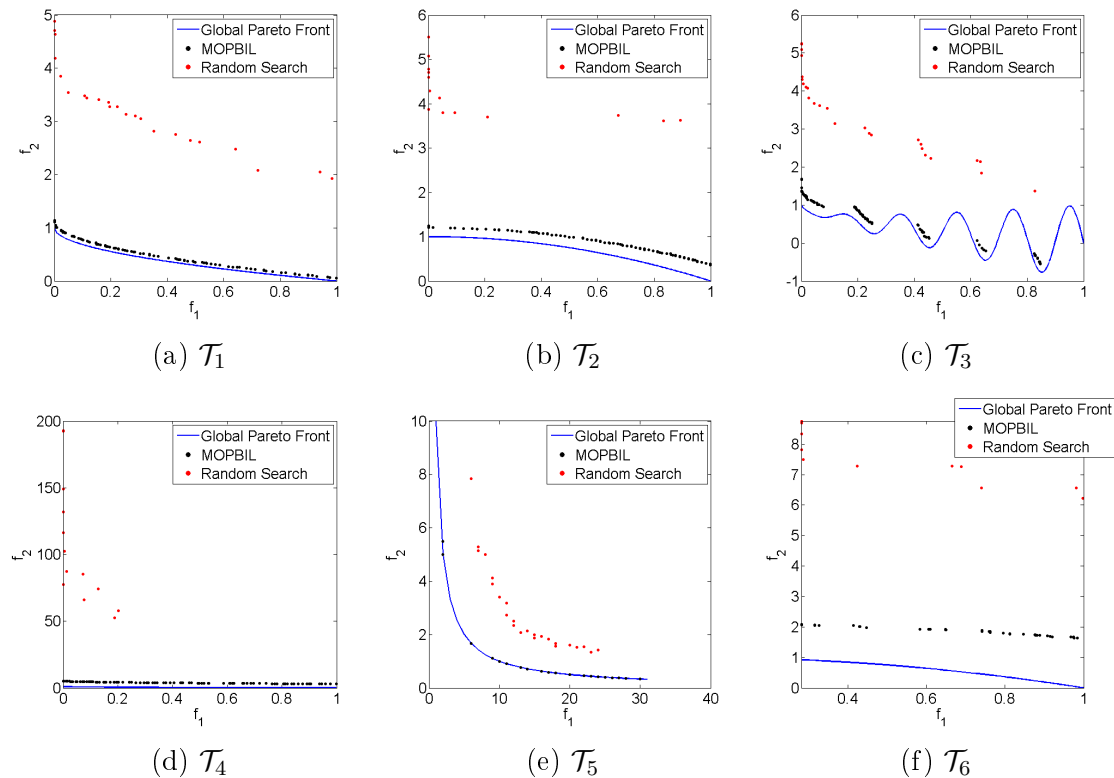
$$\begin{aligned} f_1(x_1) &= 1 - e^{-4x_1} \sin^6(6\pi x_1), \\ g(x_2 \dots x_n) &= 1 + 9 \left(\frac{\sum_{i=2}^n x_i}{n-1} \right)^{0.25}, \\ h(f_1, g) &= 1 - \left(\frac{f_1}{g} \right)^2, \end{aligned} \quad (4.11)$$

with $n = 11$, $x_1 \in [0, 1]$, and the global Pareto front was formed at $g(x_2 \dots x_n) = 1$.

4.4.2 Results

Identical optimisation parameters used for the tests as those used by Bureerat and Sriworamas [28]. The general MOPBIL parameters were 100 iterations for each optimisation with a population and maximum archive size of 100 which meant a total of 10000 function evaluations. The learning rate was set to 0.5 and the mutation probability and shift was 0.02 and 0.2 respectively. A 30 bit Gray encoding was used, unless otherwise stated, for each dimension and the probability matrix was formed using 20 probability vectors. Each probability vector was updated using 20 random archived solutions while the probabilities were limited to the interval [0.001,0.999]. Finally the adaptive grid used five bits per dimension. Figure 4.3 shows the results of the testing for both the MOPBIL algorithm and a random search. The random search was performed by simply setting the learning rate and mutation probability to zero and running MOPBIL. This meant that the probability matrix remained at the initial state with 0.5 in every position.

There are two important notes regarding the test set up. Firstly, Bureerat and Swirworamas [28] took the best result from 30 optimisations per test for each algorithm

Figure 4.3: MOPBIL and random search results on test functions \mathcal{T}_1 to \mathcal{T}_6 .

they tested. This makes sense as MOEAs are inherently stochastic and therefore prone to random perturbation in performance. In contrast the results shown in Figure 4.3 came from a single optimisation cycle. The reason was that this was simply a check to verify that the implementation worked and did so reasonably effectively and reliably.

The second note is that Bureerat and Swiroramas [28] used an additional two test functions. These were not used here because the six presented by Zitzler et al [30] provide a reasonably diverse set of tests.

The main observation from Figure 4.3 was that the MOPBIL implementation, at absolute minimum, significantly outperformed a random search of the solution space. Although this says nothing about its performance compared to other multi-objective implementations, it does at least go some way to show that it is a reasonably effective implementation. Another observation was that, in general, the results of the optimisation were close but not on the global Pareto front. This was largely due to the fact that a set number of generations was used for the test. Though this was done in order to compare this implementation against a random search, it does highlight a point that any non-exhaustive search of the solution space can only be considered an approximation at best. Monitoring changes of the adaptive grid was a possible exit criterion as it was based on the limits of the current archive. This was done for this implementation by simply including a check for the number of generation since the last

change in the adaptive grid.

Chapter 5

Multi-objective Feed Design

5.1 Introduction

A Kriging interpolate based surrogate modelling technique was investigated for use with MOO. The surrogate model construction will be described in detail and two different implementations discussed. The first interpolates directly on fine model data and the second interpolates on coarse data which would then be corrected using a regression model through a set of training points. An iterative optimisation procedure will then be described whereby the surrogate model would be corrected along the Pareto front and re-optimised if significant error was detected in a set of validation points. The technique will be applied to the optimisation of the horn described in Section 2.2.3 using different matching sections and design parameters. Results will be discussed in terms of the optimisation in general as well as specific examples from the Pareto set.

5.2 Surrogate Model

Similar to the SM experiments, the surrogate models used for the MOO used augmented coarse models. Unlike those used for the SM, the surrogate models were interpolated instead of direct simulations. As mentioned in Chapter 3, even the closed form approximation of the aperture efficiency requires the primary radiation pattern. This meant that a full wave simulation of the feed horn would be required for each direct model evaluation because no closed form method that approximates the primary radiation pattern with acceptable accuracy was available. Chapter 4.2.1 showed that MOPBIL will always require a large number of evaluations to approximate the Pareto front with any certainty of accuracy. Therefore if full wave simulation were included as part of the objective function the computational time would have been excessive. A well

established alternative is to create a surrogate model by interpolating through a limited set of evaluated solutions. This surrogate would be extremely quick to evaluate and defined over the whole solution space making it ideal as an objective function for use with MOPBIL. However there were drawbacks to this method. The interpolate would contain some error as the response from the regions between the sample points have to be estimated. The error would be correlated to the density of the data set and the smoothness of the underlying function. This also meant that enough sample points had to be included to produce an accurate interpolate. The issue with this was that the required sample density would likely not be known beforehand which meant that it would need to be estimated. Using a large number of samples could help to increase the likelihood of a converged interpolate but does not ensure it.

5.2.1 General Procedure for Model Construction

The surrogate models consisted of a Kriging interpolate [4] using a coarse model data set. The interpolate was then corrected using a regression model through a small training set. While a variety of solution spaces were used, sensitivity and reflection coefficient always constituted the final objective space. For the sensitivity surrogate model, both the coarse and fine models initially simulated the feed horn in *CST*. The farfield pattern was then extracted and the mean phase centre was computed as in Kildal [31]. The farfield pattern was then used as a feed pattern for a *GRASP* simulation with the phase centre placed directly on the focus. The fine model required that the full secondary pattern be sampled finely for the noise integration to determine the antenna temperature as discussed in Section 2.3.2. The coarse model used the mask approximation proposed by Imbriale [23] and discussed in Section 2.3.2. The surrogate model for the reflection coefficient contained no regression model because no fast approximate models were used for calculating S_{11} . The reason for this was the need for the primary pattern information meant that a full wave simulation was needed regardless and so the S_{11} data was extracted directly from the *CST* simulation. Though this is actually fine model data it will be referred to a coarse model data for further discussion because it was generally extracted from the *CST* models that formed part of the coarse data set for sensitivity. Figure 5.1 shows the various elements of the surrogate model for a two dimensional solution space.

Prior to the interpolation, the frequency dependant data obtained from the coarse and fine models needed to be reduced down to scalar values. The reason was that MOPBIL required the objective function to supply a single scalar value per objective space dimension so that Pareto dominance could be established. For the reflection coefficient this was done by taking the maximum reflection coefficient across frequency for each

solution. The sensitivity data was not only dependant on frequency but also on tipping angle. This meant that for each solution, first the mean value over tipping angle from 0° to 90° was computed for each frequency point. Then the mean of these values was computed over frequency. This was done for both the fine and coarse noise models which meant that the residuals used by the regression were already scalar. These quite simple forms of data reduction were chosen because of the smooth response they would produce.

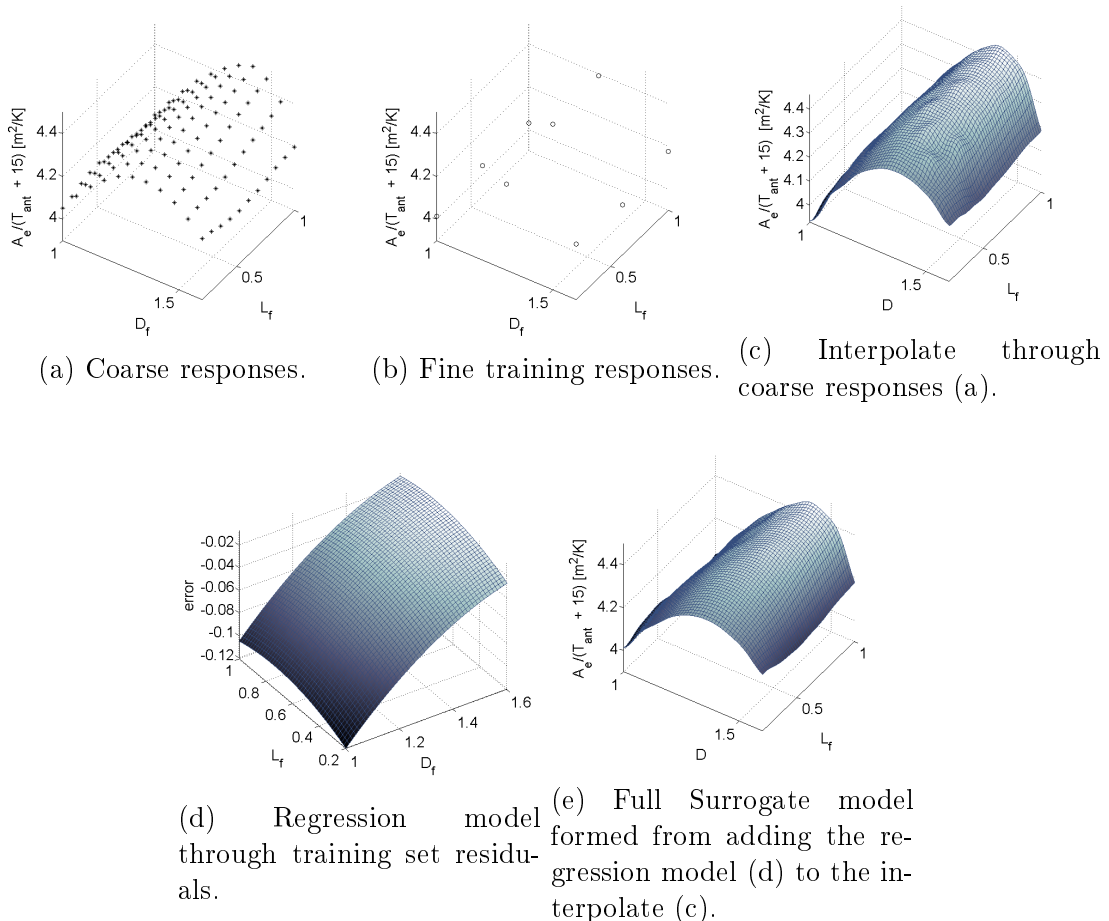


Figure 5.1: Example of different model elements constituting the sensitivity model. The reflection coefficient model would only consist of (c) and be constructed from (a)

The first task in constructing either of the surrogate models was to generate a large initial set of coarse data over the solution space. For a solution space with a small number of dimensions a course grid distribution worked particularly well for the kind of smooth response surfaces considered in this study and is shown in Figure 5.1a. For a higher dimensional solution space a grid distribution would no longer practical due to an exponential growth in the sample size. An alternative such as a Latin hypercube distribution [32] should then rather be used. To account for the error in the coarse sensitivity model an initial training set of fine and coarse data was generated in a star and corners distribution [33] shown in Figure 5.1b. For the purposes of this thesis, a star

distribution in an N dimensional solution space consists of the centre point of the solution space as well as the centre point of all the $N-1$ dimensional sides of the solution space. Again it is important to note that this was not necessary for the reflection coefficient. A Kriging interpolate was then generated for on the coarse response set, for both the sensitivity and reflection coefficient, using the *DACE* toolbox [34] for MATLAB.

The Kriging interpolate used a zero order regression model (mean) with a Gaussian correlation function. The errors between the coarse and fine responses were calculated for each point in the sensitivity training set and a regression model was fit through the residuals. Initially, a pure quadratic regression model was used but with higher dimensional solution spaces a full quadratic regression model was used to help improve the fit. A full quadratic regression model $L_{full}(x)$ contains all the linear and quadratic term in the form

$$\begin{aligned}
 x &= [x_1 \dots x_n], \\
 L_{full}(x) &= a_0 + a_1 x_1 + a_2 x_2 + \dots + a_n x_n \\
 &\quad + a_{n+1} x_1 x_1 + a_{n+2} x_1 x_2 + \dots + a_{2n} x_1 x_n \\
 &\quad + a_{2n+1} x_2 x_2 + a_{2n+2} x_2 x_3 + \dots + a_{3n-1} x_2 x_n \\
 &\quad \vdots \\
 &\quad + a_{p-3} x_{n-1} x_{n-1} + a_{p-1} x_{n-2} x_n \\
 &\quad + a_{p-1} x_n x_n,
 \end{aligned} \tag{5.1}$$

where $p = 0.5(n+1)(n+2)$ and a_0 to a_p refers to the regression constants. A pure quadratic regression model $L_{pure}(x)$ only uses the linear and square terms such that

$$\begin{aligned}
 L_{pure}(x) &= a_0 + a_1 x_1 + a_2 x_2 + \dots + a_n x_n \\
 &\quad + a_{n+1} x_1^2 + a_{n+2} x_2^2 \dots + a_{2n} x_n^2.
 \end{aligned} \tag{5.2}$$

Adding the residual regression model to the interpolate gave the surrogate model for sensitivity $R_{s,sens}(x)$ as

$$R_{s,sens}(x) = I_{sens}(x) + L_{sens}(x), \tag{5.3}$$

with $I_{sens}(x)$ referring to the interpolate through the frequency averaged coarse data set and $L_{sens}(x)$ referring to the regression model through the difference between the frequency averaged coarse data and frequency averaged fine data of the training set.

The surrogate for the reflection coefficient $R_{s,rc}(x)$ was therefore

$$R_{s,rc}(x) = I_{rc}(x), \quad (5.4)$$

with $I_{rc}(x)$ referring to the interpolate through the maximum reflection coefficient across frequency.

It is important to note that directly using fine data to generate the sensitivity was a perfectly feasible alternative. This strategy would have come with the advantage of only requiring a single interpolate like the reflection coefficient surrogate. This also could potentially be a more accurate approach because the regression model does not perfectly account for the residuals. This would have meant that the hybrid surrogate contains errors from both the interpolation and residual approximation while a pure fine response interpolation would only contain interpolation errors. The disadvantage is that the fine model is more than ten times slower than the coarse model. After the models had been streamlined, the coarse model costed, at most, approximately 78s in simulation time to evaluate a solution with 11 frequency points. The fine model would take, at most, approximately 830s to evaluate the same solution. It must be mentioned though that these are high estimates based on the highest frequency samples. This meant that a direct fine response data set would be far more size constrained in terms of data density than the hybrid model used in this study. A reduced data set would mean larger interpolation errors and less capacity for faster variation in the response surfaces.

An additional note is that because a regression model was used the training set needed to be large enough to satisfy the full rank condition. An N th order pure quadratic regression needed $2N + 1$ samples to be full rank. A star distribution training set would therefore be perfectly sufficient as it consists of $2N + 1$ samples. A full quadratic regression, of the same order, needed $0.5(N + 2)(N + 1)$ samples to be full rank.

Therefore a star distribution was insufficient and the corners need to be included. Technically, the corner samples would of been more than sufficient as it constitutes 2^N samples but this distribution lacks samples interior to the solution space.

After an initial optimisation a validation set was chosen at regular intervals along the Pareto front. Fine model evaluations were then performed on this set and compared to the corresponding surrogate responses. If a significant error existed, the surrogate model would need to be realigned. This was done by incorporating the validation set into the coarse and training data sets and regenerating the surrogate model as shown in Figure 5.2. The optimisation would then be repeated. This would continue iteratively until the error dropped to an acceptably small level. Once the error became small enough the surrogate was considered converged. A maximum error of 1 % was chosen as the

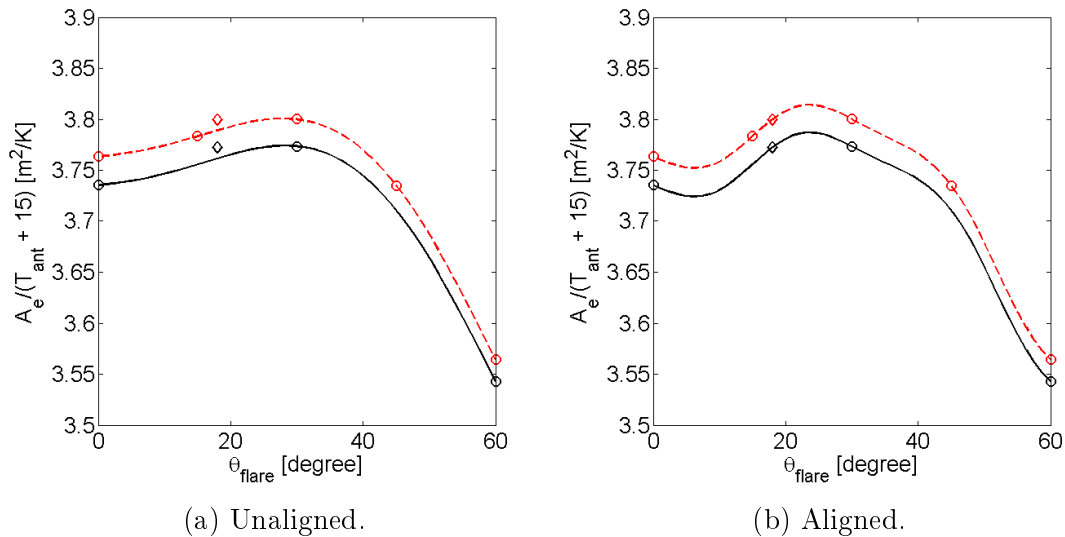


Figure 5.2: A one dimensional example of the realignment. (a) shows the unaligned model and (b) shows the aligned model. The red dotted line shows the interpolate through the coarse data points marked as red circles. The back circles represent fine training data and the black line is the surrogate response curve consisting of the interpolate and the regression model. The red and black diamonds represent coarse and fine validation data respectively.

threshold for this study.

5.3 Feed 2: Three chokes with a step

The first multi-objective optimisation was applied to a three choke horn with a step as shown in Figure 5.3. Initially three design parameters were considered for the solution space, namely flare angle (θ_{flare}), step depth (via D_f from equation (2.9)), and step length (via L_f from equation (2.10)).

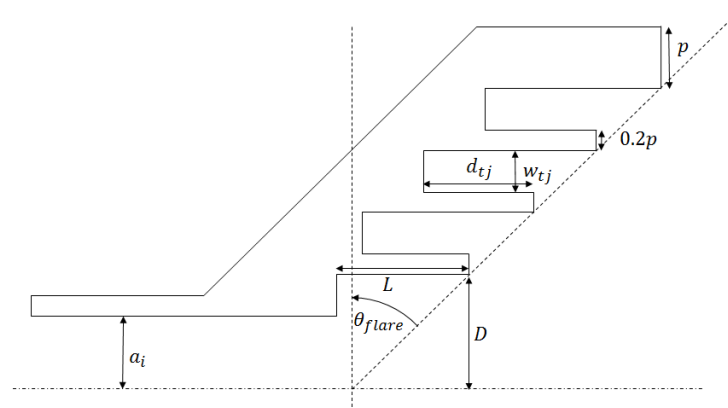


Figure 5.3: Second feed topology with three chokes and a single step

Firstly, a density for the coarse sample grid needed to be chosen. With no knowledge of

the response surfaces, this would initially be a guess at best. The problem was an initial estimate of the simulation time meant that a $21 \times 21 \times 21$ grid, which was considered a reasonable density with 9275 coarse evaluations and 14 fine evaluations, would take approximately a month of simulation time. This was not tenable due to time constraints, license issues, and power supply stability problems. Tied to this was also deciding the size of the solution space - essentially ensuring that the global Pareto set, or at least a good local Pareto set, was contained within the chosen solution space. For the flare angle there were at least reasonable limits in the sense that flare should only be forward facing, so a lower limit of 0° was required. Also, with the chokes forward facing, angles approaching 90° or larger were not realizable. The matching section was limited to a minimum depth equal to the feed waveguide and a length of zero.

5.3.1 Probing the Solution Space

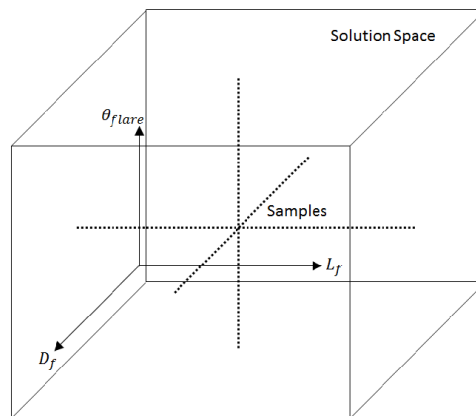


Figure 5.4: Diagram showing the sampling strategy for the initial probe of the solution space.

The issues primarily related to a lack knowledge about the response behaviour across the solution space. Therefore an initial inspection of the solution space was performed by sampling along the central axes of the three dimensional space as shown in Figure 5.4. Initial ranges for θ_{flare} , D_f , and L_f were 0° to 60° , 1 to 1.4, and 0.2 to 1 respectively. The initial probe consisted of 21 coarse evaluations and 11 fine evaluation taken along each central axis with each evaluation containing 11 frequency points. As discussed previously, the sensitivity was averaged over frequency while the reflection coefficient used the maximum across frequency. The results are shown in Figure 5.5 and Figure 5.6.

Figure 5.5a and Figure 5.6a show the sensitivity and reflection coefficient against varying flare angle. From these, the flare angle appeared to have weaker effect on both when compared to step depth and length shown in the remaining figures of Figure 5.5 and Figure 5.6. This meant that the solution space could be reduced to two dimensions, namely D_f and L_f . Additionally, the upper limit on D_f seemed to be sufficient as lower

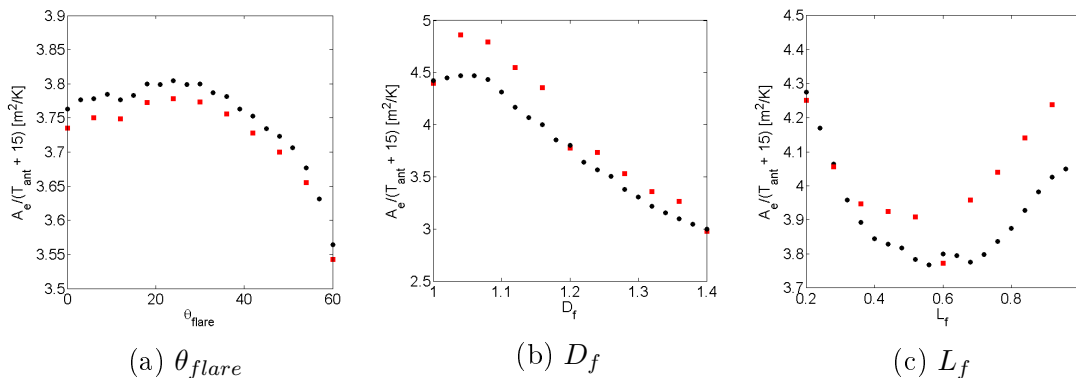


Figure 5.5: This shows the mean sensitivity along the three central axes of the solution space (a) θ_{flare} , (b) D_f , and (c) L_f . The red squares show fine model evaluations while the black dots are coarse model evaluations.

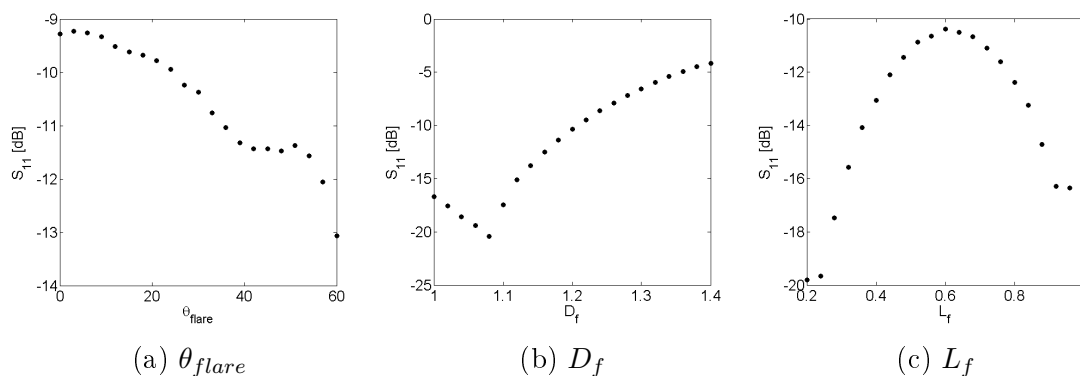


Figure 5.6: The maximum reflection coefficient across frequency along each of the three central axes (a) θ_{flare} , (b) D_f , and (c) L_f of the solution space.

values were favoured by both sensitivity and reflection coefficient. The step length showed an unfortunate bias towards the edges of the range. The upper limit already constituted two feed waveguide radii and making it any longer would start turning it from a matching section to a de facto feed guide. Therefore the limits were retained for the initial surrogate construction.

5.3.2 Characterizing the Objective Space

From the initial probe of the solution space the flare angle (θ_{flare}) was fixed at 30° and the first surrogates were constructed. The opportunity was taken to gain more insight into the objective space. From Figure 5.7, it could be seen that a ridge of peak sensitivity could be found with a shallow D_f of between 1.05 and 1.1 and an arbitrary L_f limited to the original range. The sensitivity declined sharply toward the corner of the solution space representing long deep steps. Increased overmoding of the step section is the likely cause which is to be expected as the cut off for the TM_{11} mode in

the feeding wave guide was 1.56 GHz, only slightly above the 1.5 GHz upper edge of the band. Therefore any value of D_f larger than 1.04 means that the TM_{11} mode could propagate in the step at the higher end of the band.

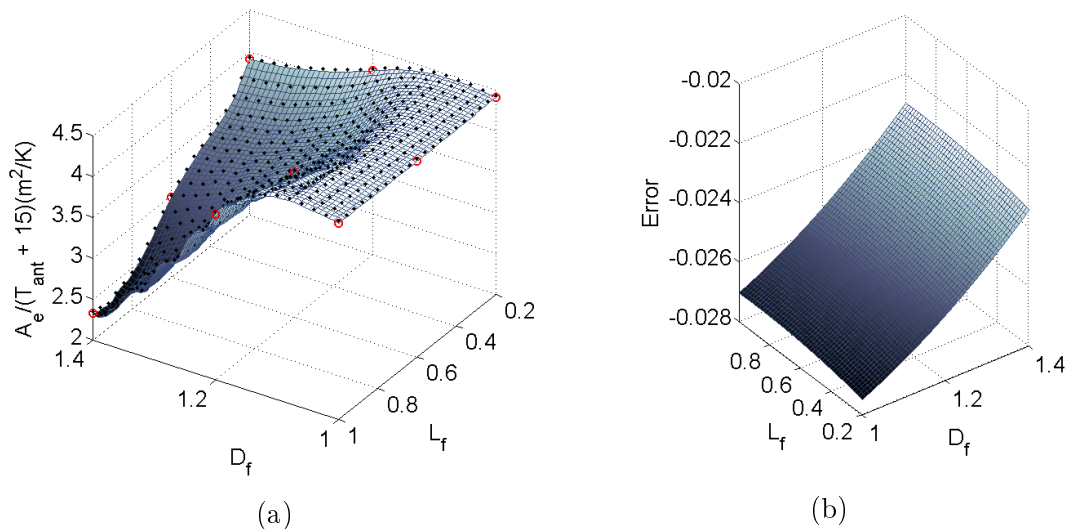


Figure 5.7: (a) The sensitivity surrogate response surface for stepped horn profile is shown by the surface. The black dots show the original coarse data while the fine training data is shown by the red circles. (b) The response surface of the regression model to correct some of the coarse data error.

The response surface for the reflection coefficient is shown in Figure 5.8. A initial observation was that this profile was not particularly well matched across most of the solution space. The minimum reflection coefficient possible was only slightly below -20 dB while the maximum sat above -5 dB. As a point of comparison, the mean of the reflection coefficient over frequency was computed for each point in the original coarse data set and is shown as green dots in Figure 5.8. The large difference that could be seen between the surrogate, which represented the maximum reflection coefficient, and these mean values indicated that the reflection coefficient of the stepped feed was generally very sensitive to frequency. This was largely attributed to a single step being a fairly narrow band matching structure. The poor performance of the stepped feed with regard to reflection coefficient over the solution space prompted the use of a linear taper rather than a step in a third horn profile.

5.3.3 Optimisation Results

For the optimisation, a population of 100 was used with a maximum and minimum archive of 200 and 20 respectively. A 10 bit Gray encoding scheme was used for each solution space dimension while the adaptive grid used a 5 bits binary encoding scheme

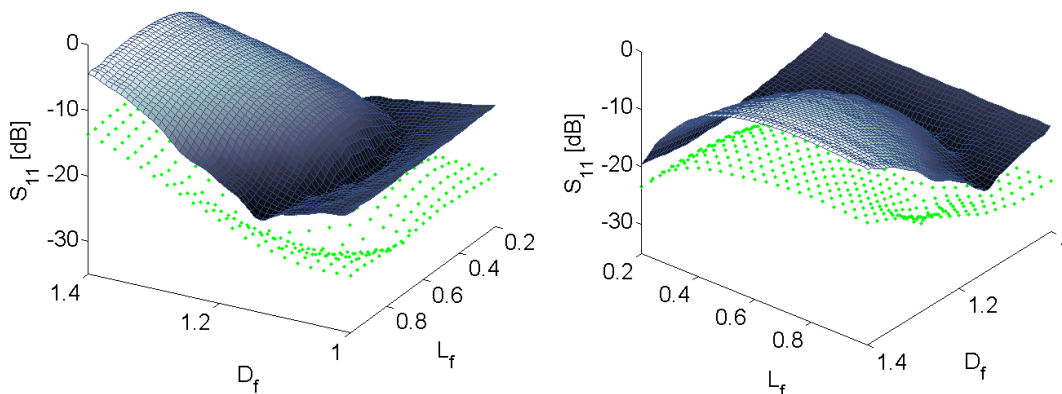


Figure 5.8: The reflection coefficient surrogate (maximum over frequency) response surface for second horn is shown as the surface. The green dots show the mean over frequency of the reflection coefficient calculated from the original frequency dependant coarse data set. The two plots are identical, only with different orientations.

for each solution space dimension. The probability matrix was formed using 50 probability vectors and trained using 20 archived solutions per vector. The learning rate was set to 0.3 while the mutation probability and shift were set to 0.02 and 0.2 respectively. The exit criterion was no change of adaptive grid for 50 generations. With these parameters a high degree of exploration was expected with a well filled front.

Multiple runs were performed with consistent results to ensure that the optimisation parameters were producing a good approximate Pareto front. Figure 5.9 shows the final optimisation results.

The first generation validation set constituted ten solutions which are shown by the red circles in Figure 5.9 and listed in Table A.2 in Appendix A. The maximum error in the validation set was 0.8809 % for the sensitivity and 0.8532 % for the reflection coefficient with mean error values of 0.367 % and 0.3996 % respectively. Therefore no additional alignment and optimisation iterations were required.

From Figure 5.9a, the peak sensitivity achievable for the stepped horn profile was approximately $4.49 \text{ m}^2/K$ while the minimum reflection coefficient was approximately -21 dB which was expected from the initial characterization of the solution space. The sensitivity range for the Pareto front was quite small at $0.12 \text{ m}^2/K$, which was 2.67 % of the peak value while the reflection coefficient range was 2.25 dB, or 10.71 % of the peak value which was larger than the sensitivity but still quite small. Looking at Figure 5.9b, the Pareto set was quite condensed as well with the values of D_f only varying by approximately 0.07 around a value of 1.1 and values of L_f concentrating around values of 0.99 and 0.58. Unfortunately this meant that the Pareto set was largely up against

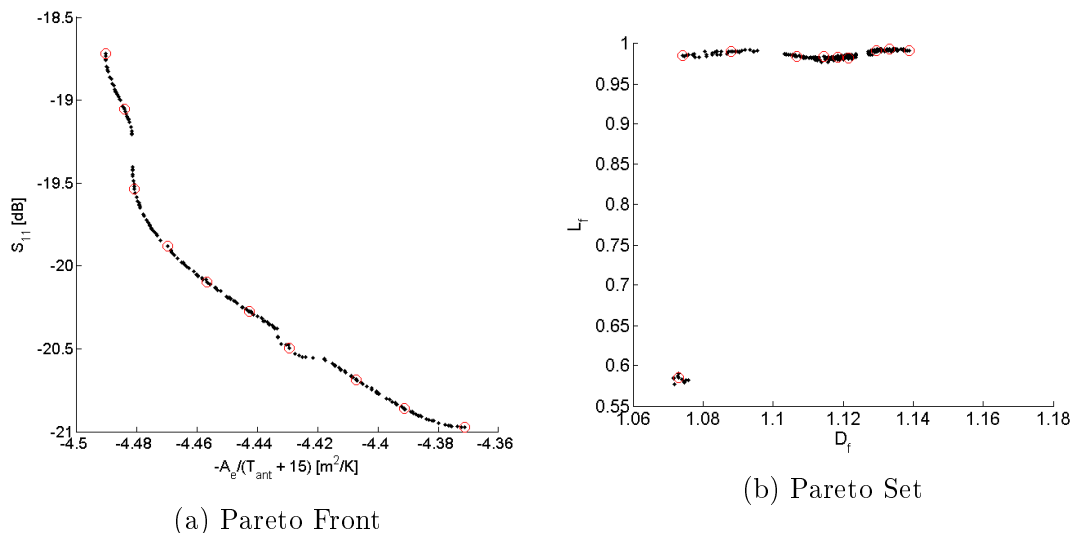


Figure 5.9: Optimisation results for the stepped horn profile with (a) the Pareto front and (b) the Pareto set. Black dots show the surrogate results while the red circles show the solutions chosen for validation.

the upper limit of L_f which meant that the decision not to increase this prior to the surrogate construction was a poor one. This was not expected as more spread was anticipated along the trough in the reflection response surface seen in Figure 5.8 because a ridge of maximum sensitivity was found in the same region. To help visualize this, the Pareto set was plotted onto both of the response surfaces as shown in Figure 5.10. It revealed that two troughs in the reflection coefficient response surface seem to define the Pareto set. This is understandable as both represent regions of minimum reflection coefficient that sit on, or near too, the reasonably smooth ridge of maximum sensitivity in the sensitivity response surface. Figure 5.10 also highlights a fact that there was a slight gradient on that ridge favouring a longer step sections. Ideally, the solution space should have been expanded, the surrogates rebuilt, and the optimisation rerun. Unfortunately, because of the poor reflection coefficient response, the focus had already shifted to the tapered profile. Regardless of this, the stability of the optimisation results over multiple runs indicated that this was a close approximation to the global Pareto front for the solution space given the current surrogate model.

SLL was not an explicit objective parameter but the data needed to generate an interpolate was the same as the reflection coefficient. The SLL was simplified to a scalar for each point in the coarse data set by taking the mean over frequency. Figure 5.11 shows the response surfaces for the first (SLL_1) and second (SLL_2) side lobe level with the Pareto set plotted onto each. These figures showed the SLL became quite sensitive to deeper steps. This is indicative of a higher order mode beginning to propagate within the step. Although mode mixing is a well established means of generating a near ideal aperture field distribution [35], the purpose of the step here was to allow for variation in

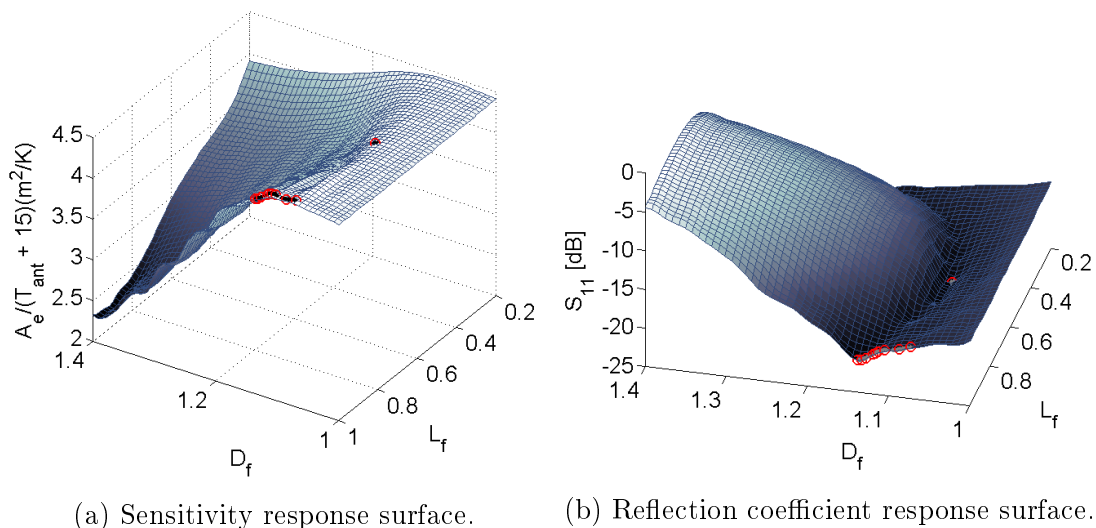


Figure 5.10: The Pareto set plotted as (a) black dots on the sensitivity response surface and (b) as grey dots on the reflection coefficient response surface. The red circles in both represent the validation set.

the radius of the throat of the horn.

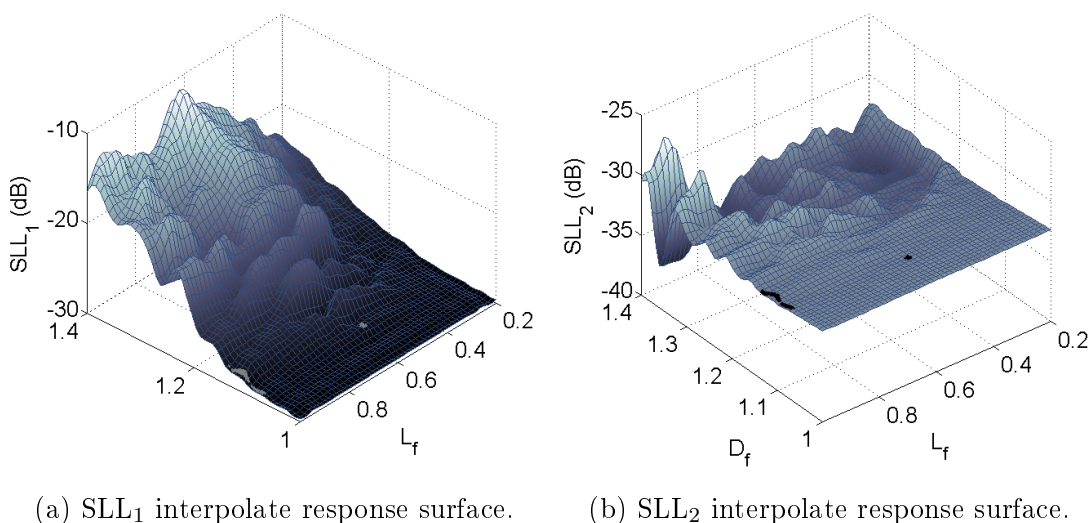


Figure 5.11: The Pareto set plotted onto the (a) SLL_1 interpolate response surface as grey dots and (b) SLL_2 interpolate response surfaces as black dots. Both the SLL_1 and SLL_2 values are averages over frequency.

5.3.4 Case study

As discussed in Section 5.2.1, the models used for optimisation comprised a large amount data simplification which meant that the frequency dependant behaviour of the

solutions as largely masked. Aspects such as resonances and the subtler effects of overmoding in the waveguide sections could not really be discerned from the surrogate response surfaces and certainly not from the Pareto front or set. For this reason, Table 5.1 lists three solutions that were chosen for further examination. These included solutions from both edges of the Pareto front as well as a third solution from the interior of the Pareto front. It must be noted that the best sensitivity solution (S_1) was chosen from the validation set based on the fine response. This meant that it was not a solution on the edge of the Pareto front, as shown by Table A.2 in Appendix A. The error was likely due to the limited range in the sensitivity dimension and concave shape of the Pareto front which meant that the region near the peak sensitivity edge of the front was very sensitive to the small errors that still existed in the surrogate. The interior solution was chosen to be representative of the smaller grouping of solutions in the Pareto set seen around $L_f = 0.58$ in Figure 5.9b. This did mean that this compromise solution (C_1) favoured reflection coefficient over sensitivity. Finally the best match solution (M_1) was chosen for the lowest reflection coefficient out of the validation sets. The profiles of these three solutions are shown in Figure B.1 in Appendix B.

Table 5.1: Three stepped profile solutions chosen from the validation set in Table A.2 for further investigation. The short hand for each solution is indicated in brackets.

	D_f	L_f
Best Sensitivity (S_1)	1.09	0.991
Compromise (C_1)	1.07	0.586
Best Match (M_1)	1.14	0.991

Figure 5.12 and Figure 5.13 show the sensitivity and reflection coefficient over frequency for the three examples. The initial observation was that, for the surrogate response over the Pareto set, the upper region of the band largely decided the surrogate sensitivity response while the lower edge of the band largely decided the surrogate reflection coefficient response. Additionally, the S_1 solution does not display the highest levels of sensitivity over a large region of the band. It does however show less degradation at the upper end of the band and therefore a higher mean value. A final observation was that the lower region of the band was generally less volatile for both sensitivity and match.

In order to get better insight into what was causing this further parameters were investigated.

As sensitivity is largely dependant on the shape of the primary feed pattern, a stable feed pattern over frequency is important for stable sensitivity over frequency. A good measure of radiation pattern stability is maximum gain over frequency. The maximum gain over frequency of the primary pattern, as generated by the feed horn, is shown in Figure 5.14 for all three solutions. A monotonic rise in maximum gain with frequency

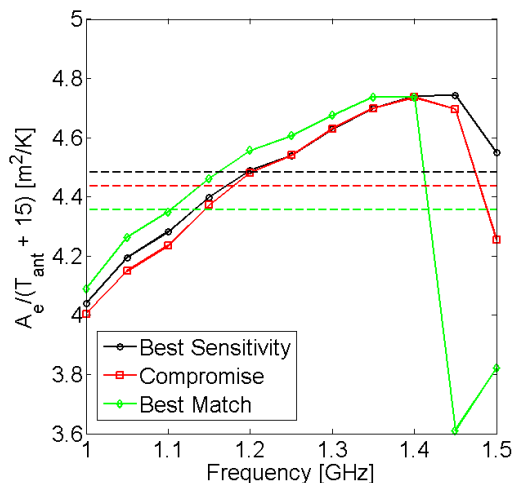


Figure 5.12: The solid lines with markers show the sensitivity over frequency for the three solution in Table 5.1. The dashed lines show the mean values that would be used by the surrogate. The black traces refer to the S_1 , the red to the C_1 , and the green to the M_1 .

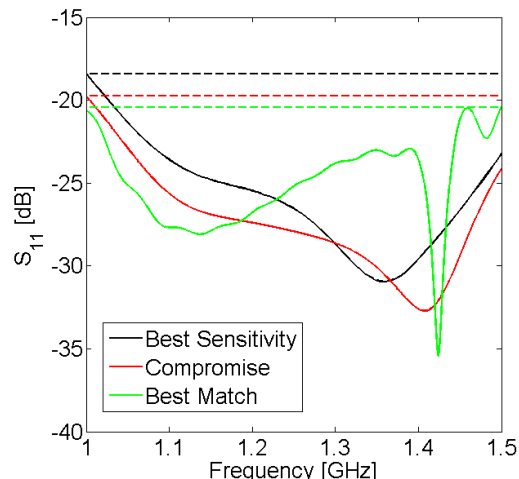


Figure 5.13: The solid lines plot the reflection coefficient over frequency. The dashed lines show the maximum values that would be used by the surrogate. The black traces refer to the S_1 , the red to the C_1 , and the green to the M_1 .

was expected due to the horn appearing electrically larger at higher frequencies. All three solutions are reasonably smooth over the lower half of the band. The faster variation in the upper half of the band was most likely due to the TM_{11} mode beginning to propagate because D_f was larger than 1.04, as discussed in Section 5.2.1. This is further evidenced by the variations becoming more pronounced with larger values of D_f , as exemplified by M_1 . It was expected that this inconsistency in the feed pattern would translate into a degradation of the aperture efficiency, which was subsequently seen in Figure 5.15. The effect of this primary pattern instability could also be seen in raised antenna temperature levels over the upper region of the band for M_1 shown in Figure 5.16. Similarly, being significantly less effected by the overmoding, the smoother responses of the other two solutions translated to better aperture efficiency and antenna temperature over the upper end of the band. The first and second side lobe levels were similar for three solutions, particularly SLL_2 , and can be seen in Figure 5.17 and Figure 5.18.

An interesting note is that the reflection coefficient towards the lower edge of the band improved with larger values of D_f . This was not seen in the response surface shown in Figure 5.10b because the reflection coefficient over the upper region of the band degraded heavily with larger values of D_F . A final observation was that in Figure 5.12 the sensitivity was increasing monotonically from 1 GHz to approximately 1.4 GHz. Lower antenna temperatures without significant loss of aperture efficiency seems to be the reason for this and indicated that a larger throat might have been better, had the

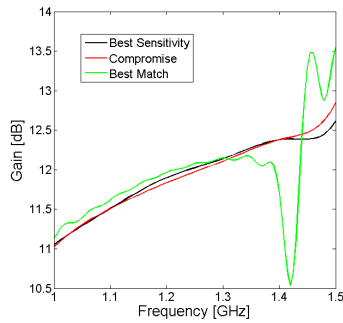


Figure 5.14: Maximum gain over frequency of the primary pattern generated by the three example solutions. The black trace refers to S_1 , the red to C_1 , and the green to the M_1

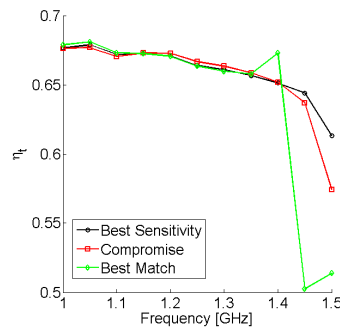


Figure 5.15: Aperture efficiency over frequency for the whole reflector system. The black trace refers to S_1 , the red to C_1 , and the green to M_1 .

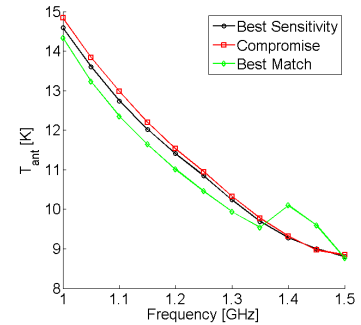


Figure 5.16: Antenna temperature averaged over tipping angle versus frequency for the whole reflector system. The black trace refers to S_1 , the red to C_1 , and the green to M_1 .

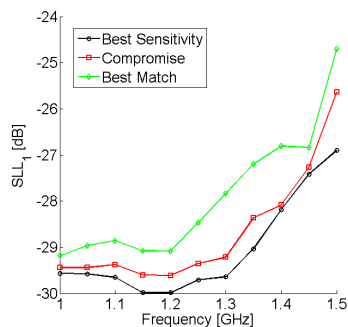


Figure 5.17: SLL_1 over frequency of the secondary pattern. The black trace refers to S_1 , the red to C_1 , and the green to M_1 .

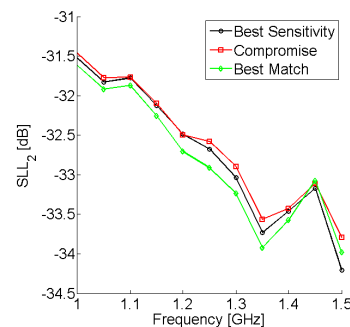


Figure 5.18: SLL_2 over frequency of the secondary pattern. The black trace refers to S_1 , the red to C_1 , and the green to M_1 .

higher mode propagation not been an issue. This was further evidenced by M_1 , which actually shows slightly better sensitivity from 1 GHz to 1.35 GHz than the other two examples. Alternatively larger flare angles may also have had a similar effect.

5.4 Feed 3: Three chokes with a linear taper

A third feed design was explored with the profile shown in Figure 5.19. It was essentially the same feed horn as that used in Section 5.3 but with the step replaced by a linear taper. This was done in an attempt to improve the reflection coefficient over the solution space. At this point some refinement of the various simulations had also taken place that significantly reduced the computation time. The main improvement came from fixing the size of the mesh and disabling the automatic convergence feature for

GRASP. The adaptive meshing algorithm was very efficient but still required multiple iterations per simulation. The mesh density for the system was set to be slightly larger than the typical mesh density for a simulation at 1.5 GHz which had been noted from previous simulations. This roughly halved the overall simulation time from 148 s down to 78 s per coarse evaluation and from 1787 s down to 830 s per fine evaluation. It must again be noted that these are a slight overestimation based on the simulation time of the highest frequency components.

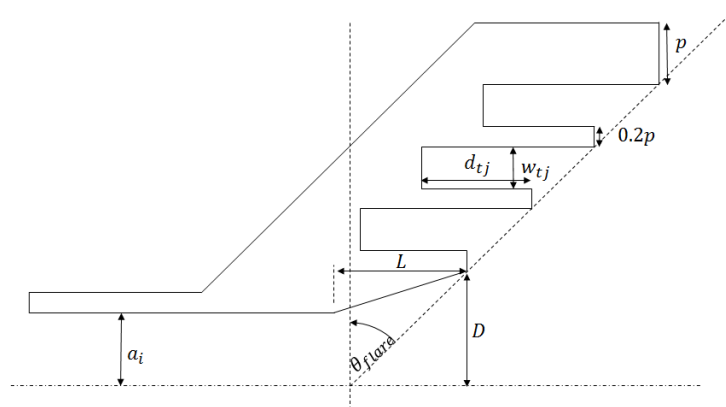


Figure 5.19: Third feed topology with three chokes and a linear taper

5.4.1 Two dimensional solution space

For the initial optimisation of the tapered profile a two dimensional solution space was used. Though this profile used a different matching section to the stepped profile in Section 5.3 the design parameters were identical. The taper was therefore fully defined by D and L which were modified by D_f and L_f respectively as shown by equations (2.9) and (2.10). The solution space was therefore similar to the one used for the stepped profile with the ranges for D_f and L_f chosen as 1 to 1.6 and 0.2 to 1 respectively. The same optimisation parameters were used as those in Section 5.3.3 for the stepped profile optimisation except that each probability vector was trained on 25 archived solutions. This was done to improve the exploration of the solution space. Figure 5.20 shows the resulting Pareto front. The change to a tapered matching section yielded a marginal increase in the lower limit of the sensitivity range compared to the stepped profile. The reflection coefficient however saw a general improvement across the Pareto front as well as a substantial increase in range from 2.5 dB for the stepped profile to over 10 dB for the tapered profile though the region of the Pareto front favouring the match was sparsely populated. The accompanying Pareto set can be seen in Figure 5.21 and here again far more variation was found when compared to the stepped profile. Additionally,

despite some solutions near the borders, the majority of the Pareto set was more internal to the solution space.

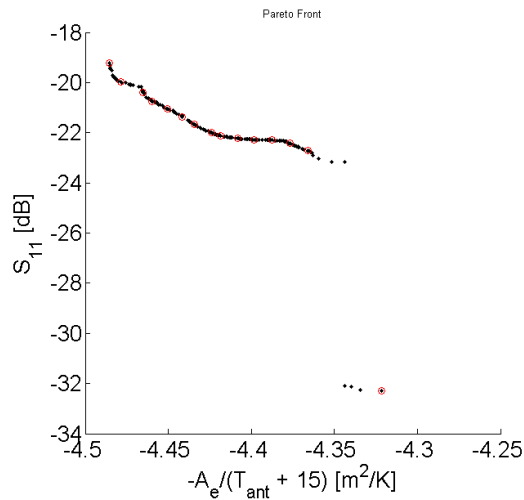


Figure 5.20: The Pareto front plotted as black dots for the tapered profile with a two dimensional solution space. The validation set is mark by red circles.

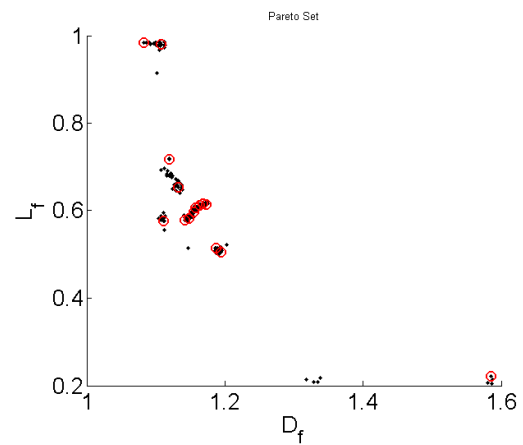


Figure 5.21: The Pareto set plotted as black dots for the tapered profile with a two dimensional solution space. The validation set is mark by red circles.

Figure 5.22 and Figure 5.23 shows the response surfaces for the sensitivity and reflection coefficient respectively. The Pareto set has been plotted onto each to show some of the contours that the it adhered to. The sensitivity response surface looked similar to that of the stepped profile. This was expected because the aperture side of the horn was the same so the radiation characteristics were largely unchanged. Conversely, the reflection coefficient response surface differed significantly showing substantial improvement in the regions constituting deep tapers and especially in the region constituting short, deep tapers. In particular it showed a -30 dB reflection coefficient in the region of very short and very deep tapers. This was most likely due to a better reflection coefficient at the lower edge of the band due to the large throat of the horn while the short, steep taper prevented significant propagation of higher order modes. Interestingly, the cut-off frequency for the TM_{11} mode with $D_f = 1.6$ was 0.976 GHz which meant that had this been a stepped matching section the TM_{11} mode could of actually propagated across the entire band. With less of a discontinuity than the step, the taper seems to limit the generation and propagation of these higher order modes.

From the shape of the response surfaces it was expected that the sensitivity response would drive the optimisation toward a long shallow taper while the reflection coefficient would drive toward a short deep taper. This was what could be seen in Figure 5.22 and Figure 5.23. Interestingly, the shallow valley on the short taper edge of the sensitivity response surface actually creates a discontinuity in the Pareto front. As with

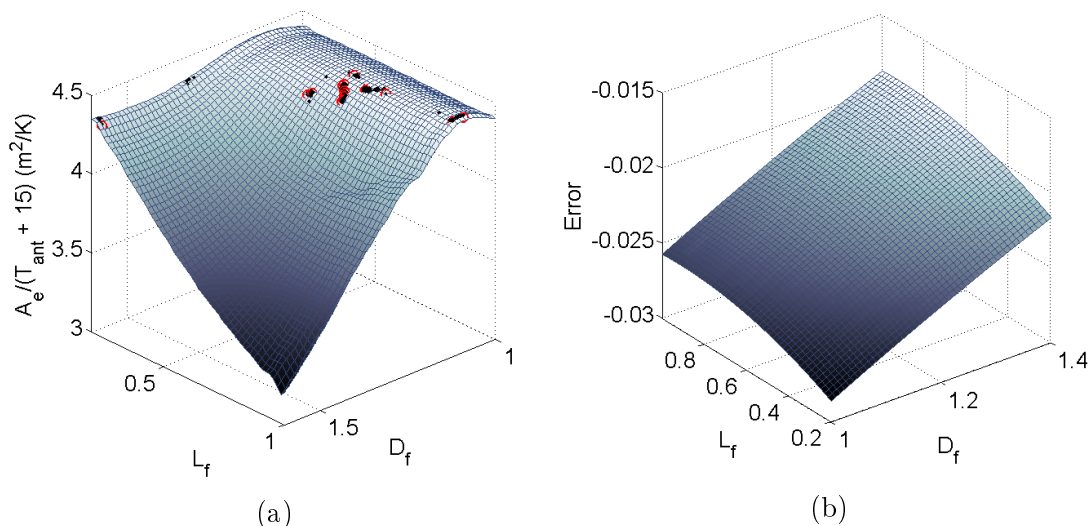


Figure 5.22: (a) The Pareto set plotted as black dots onto the sensitivity response surface of the tapered profile with a two dimensional solution space. The validation set is mark by red circles. (b) The response surface of the regression model used to correct some of the coarse model errors.

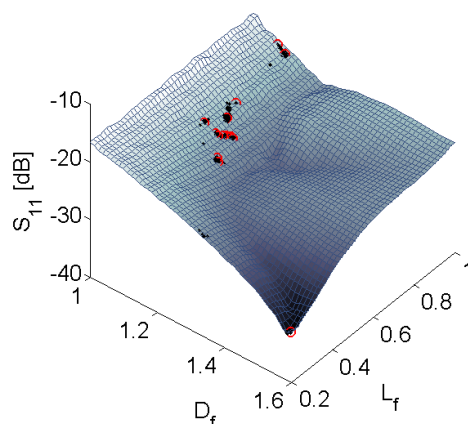


Figure 5.23: The Pareto set plotted as black dots onto the reflection coefficient response surface of the tapered profile with a two dimensional solution space. The validation set is mark by red circles.

the stepped profile, multiple optimisation runs were performed without realignment to check that the optimisation parameters were stringent enough to produce stable results. This was the case but unfortunately the small non-contiguous region remained sparsely populated.

The SLL_1 response was similar to that of the stepped profile but with a smoother response surface as could be seen in Figure 5.24. As with the reflection coefficient, this was most likely due to far less propagation of the higher order modes. A similar case could be seen in the SLL_2 response shown in Figure 5.25. For both of these responses

the regions of highest variation were in the region of long deep tapers where propagation of higher order modes would be expected.

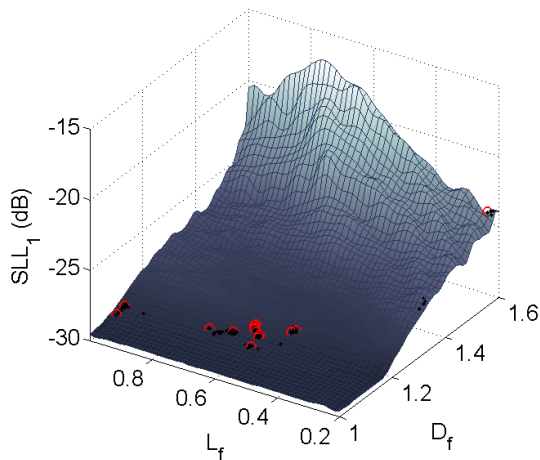


Figure 5.24: The Pareto set plotted as black dots onto the SLL_1 response surface of the tapered profile with a two dimensional solution space. The validation set is mark by red circles.

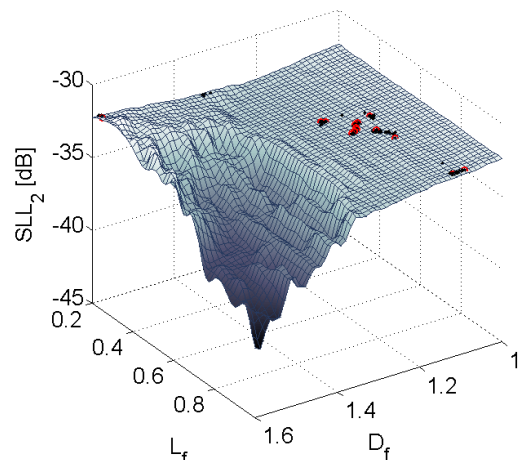


Figure 5.25: The Pareto set plotted as black dots onto the SLL_2 response surface of the tapered profile with a two dimensional solution space. The validation set is mark by red circles.

A 15 point validation set was chosen similarly to Section 5.3.3 and is indicated by red the red circles in Figure 5.22 to Figure 5.25. The results are shown in Table A.3 in a Appendix A. The highest error in sensitivity was 0.332 % with a mean error of 0.107 % while the reflection coefficient showed a maximum error of 0.432 % and a mean error of 0.219 %. With such small errors no additional iterations of realignment and optimisation were required. It is interesting to note that the error seen here was far smaller than that seen with the stepped profile. This apparent alignment may simply be a sampling anomaly or it may have stemmed from the purer single mode operation of this profile leading to smoother variations in sensitivity and reflection coefficient.

5.4.2 Three dimensional solution space

An optimisation on the tapered profile with a three dimensional solution space was also attempted. The flare angle θ_{flare} was added to D_f and L_f to form the dimensions of the solution space. The range for the taper dimensions were kept the same as those for the two dimensional space while the range for the flare angle was from 0° to 60° . A grid distribution was once again used with 11 divisions per dimension and 11 frequency points per sample. This meant a coarse data set of 1331 samples plus an additional 14 training points. Six of the training points were not already included in the coarse set so,

in total, 1337 coarse evaluations and 14 fine evaluation were required for the initial surrogate construction.

The same optimisation parameters were used as before but the population size was increased to 300 to improve exploration in the larger solution space. Again several optimisation runs were performed in order to check that the results were stable. Figure 5.26 and Figure 5.27 show the results obtained.

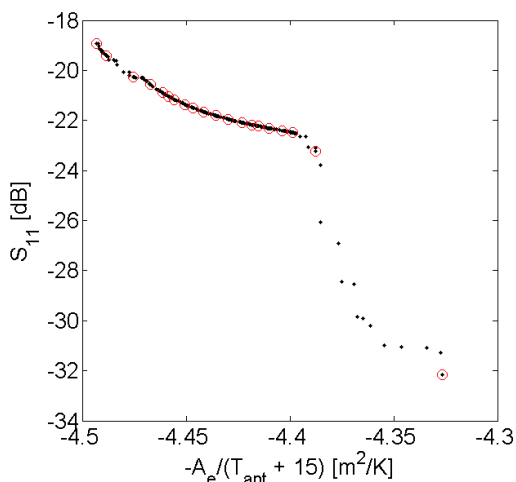


Figure 5.26: The Pareto front from the optimisation of the tapered profile with a three dimensional solution space represented as black dots. The red circles show the validation set.

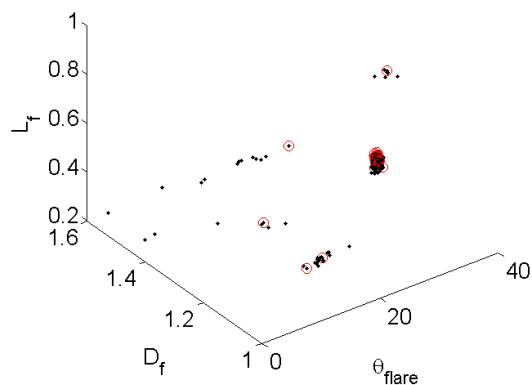


Figure 5.27: The Pareto set from the optimisation of the tapered profile with a three dimensional solution space shown as black dots. The validation set is represented by red circles.

The Pareto front looked similar to that obtained from the two dimensional solution space in Section 5.4.1. While there was less of a discontinuity, the contiguous and non-contiguous regions were similarly placed. The range of the Pareto front, in terms of objective space dimensions, was also similar to that of the Pareto front in Section 5.4.1. Additionally, the Pareto set, when projected onto the $L_f - D_f$ plane, is contained in similar regions to the Pareto set from the two dimensional solution space in Section 5.4.1. This seems to suggest that either the flare angle had minimal effect on the response or that the effect of the flare angle was fairly uniform over the $L_f - D_f$ plane and a flare angle of 30° was close to the optimum. The 18° of range along θ_{flare} seen in the Pareto set suggest the former.

Again a validation set was generated and is shown as red circles in Figures 5.26 and Figure 5.27. The results are shown in Table A.4 in Appendix A. The sensitivity showed a peak error of 0.446 % and a average error of 0.142 % while the reflection coefficient showed a peak error of 0.445 % and a mean error of 0.0925 %. As with the previous cases the residual error was small enough not to warrant an additional alignment and

optimisation iteration.

5.4.3 Case Studies

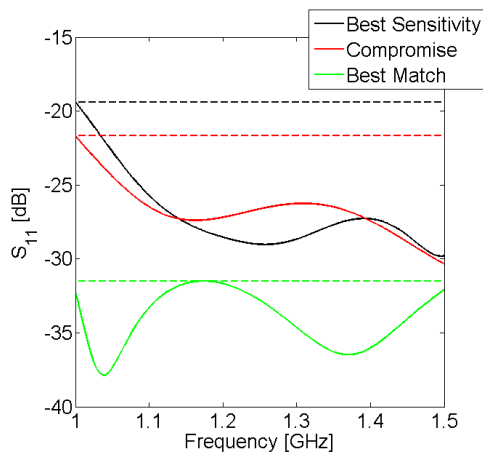
Table 5.2: Three tapered profiles chosen from the two dimensional validation set, shown in Table A.3, for further investigation. The short hand for each solution is indicated in brackets.

	D_f	L_f
Best Sensitivity (S_2)	1.08	0.984
Compromise (C_2)	1.15	0.598
Best Match (M_2)	1.58	0.221

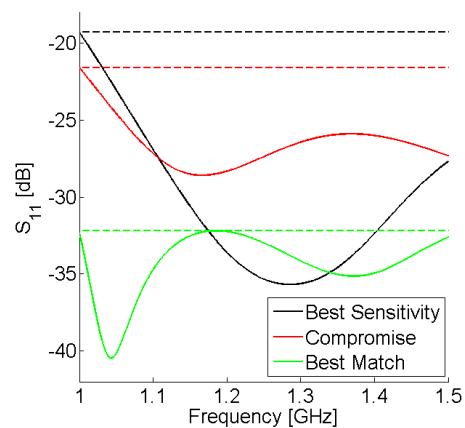
Table 5.3: Three tapered profiles chosen from the three dimensional validation set, shown in Table A.4, for further investigation. The short hand for each solution is indicated in brackets.

	θ_{flare}	D_f	L_f
Best Sensitivity (S_3)	18.7	1.17	0.232
Compromise (C_3)	26.5	1.15	0.581
Best Match (M_3)	33.5	1.59	0.206

As with stepped profile in Section 5.3.4 some specific solutions were chosen for closer investigation. Three solutions were chosen from both the two dimensional Pareto set in Section 5.4.1 and three dimensional Pareto set in Section 5.4.2 with the chosen solutions appearing in Table 5.2 and Table 5.3. Again these consisted of best sensitivity (S_2 and S_3), best match (M_2 and M_3), and compromise (C_2 and C_3) solutions with the associated profiles shown in Figure B.2 and Figure B.3 in Appendix B.



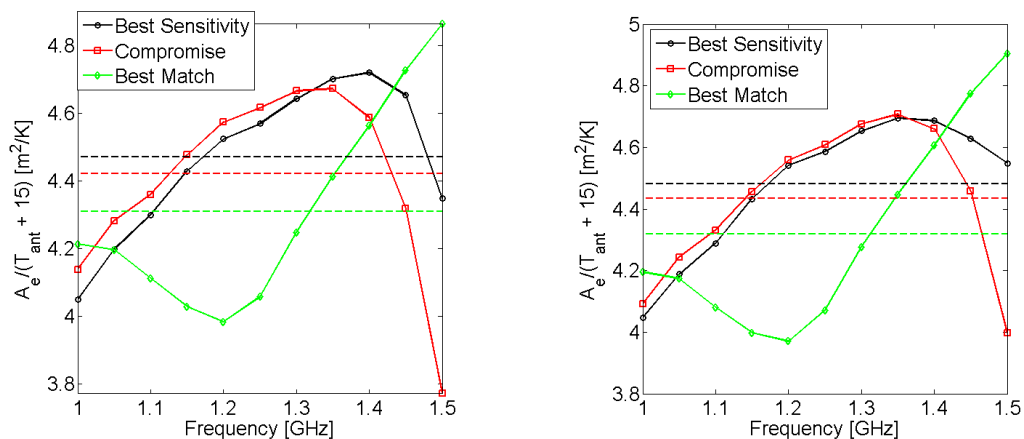
(a) Two dimensional solutions.



(b) Three dimensional solutions.

Figure 5.28: The reflection coefficient over frequency is shown for (a) the two dimensional solutions and (b) the three dimensional solutions. The best sensitivity solutions S_2 and S_3 are represented by black traces while the compromise solutions C_2 and C_3 are represented by red traces and the best match solution M_2 and M_3 are represented by green traces. The solid line represent the frequency response while the dashed lines show the simplified surrogate response (maximum over frequency) for the solutions.

An initial observation was that the corresponding solutions from the two and three dimensional solution spaces showed similar responses over frequency as could be seen in Figure 5.28 to Figure 5.31. Another interesting note is that the sensitivity responses of S_2 , S_3 , C_2 , and C_3 shown in Figure 5.29 bore some similarity to the sensitivity pattern of all three stepped profile solutions S_1 , C_1 , and M_1 shown in Figure 5.12. This could be attributed to all seven solutions using similar values of D_f which meant that their primary feed patterns were similar. The best match solutions M_2 and M_3 differed significantly from all the other solutions which was likely due to the deep, short taper of these solutions. Considering the reflection coefficient seen in Figure 5.28 lends support to the assertion made in Section 5.4.1 that the deep throat (large D_f) allowed for lower reflection coefficients at the lower edge of the band while the short taper seemed to minimize the deleterious effects of the matching section becoming overmoded on the reflection coefficient towards the upper edge of the band.



(a) Sensitivity over frequency for the two dimensional solutions.

(b) Sensitivity over frequency for the three dimensional solutions.

Figure 5.29: The sensitivity over frequency is shown for (a) the two dimensional solutions and (b) the three dimensional solutions. The best sensitivity solutions S_2 and S_3 are represented by black traces while the compromise solutions C_2 and C_3 are represented by red traces and the best match solution M_2 and M_3 are represented by green traces. The solid line represent the frequency response while the dashed lines show the simplified surrogate response (mean over frequency) for the solutions.

Comparing the maximum gain of the primary feed pattern in Figure 5.30a and Figure 5.30d and the aperture efficiency of the total system in Figure 5.30b and Figure 5.30e it could be seen from solutions S_2 , S_3 , C_2 , and C_3 that the peak aperture efficiency was achieved when the feed pattern had a maximum gain of approximately 11 dB to 12 dB depending on frequency. Figure 5.30a and Figure 5.30d also showed that M_2 and M_3 generated a relatively consistent primary pattern, at least in terms of maximum gain. However, these also showed that M_2 and M_3 showed a peak primary pattern gain of over

12 dB for the whole band which meant that the aperture efficiency was significantly lower due to poor illumination efficiency. This did produce lower antenna temperatures over the lower half of the band but these were not enough to compensate for the compromised aperture efficiency resulting in the low sensitivity.

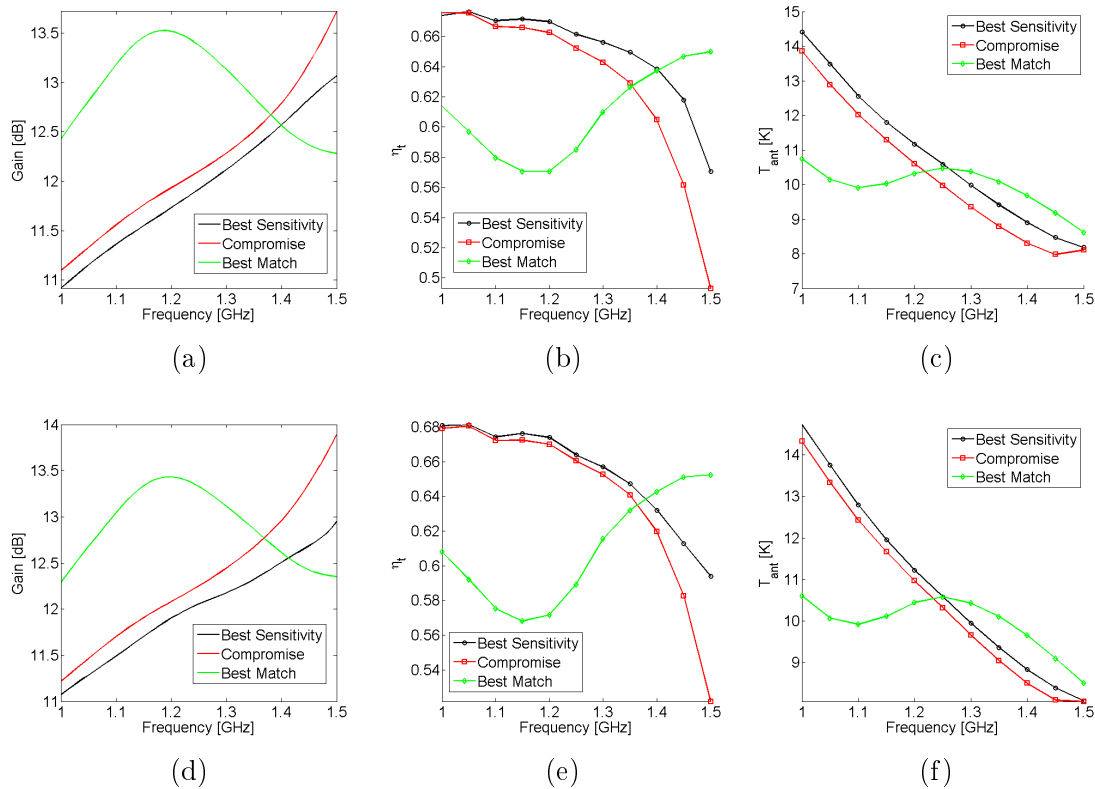


Figure 5.30: Above is shown maximum gain over frequency of the primary feed patten for (a) the two and (d) the three dimensional solutions. The aperture over frequency efficiency of the whole reflector system for (b) the two and (e) three dimensional solutions and the antenna temperature over frequency for (c) the two and (f) three dimensional solutions are also shown. The best sensitivity solutions S_2 and S_3 are represented by black traces while the compromise solutions C_2 and C_3 are represented by red traces and the best match solution M_2 and M_3 are represented by green traces.

Despite the smooth aperture efficiency and antenna temperature, M_2 and M_3 showed significant increase in SLL_1 particularly around 1.2 GHz as seen in Figure 5.31a and

Figure 5.31d. This coincides with the peek in maximum gain of the primary feed pattern and the trough in aperture efficiency. The precise cause of this was not entirely clear as the drop in aperture efficiency was primarily due to under illumination of the aperture. This would imply lower edge illumination and therefore lower SLL.

Additionally, the polarisation, phase, and diffraction efficiencies, which could all relate to raised SLL, were all well above 90 % indicating that these were likely not the cause.

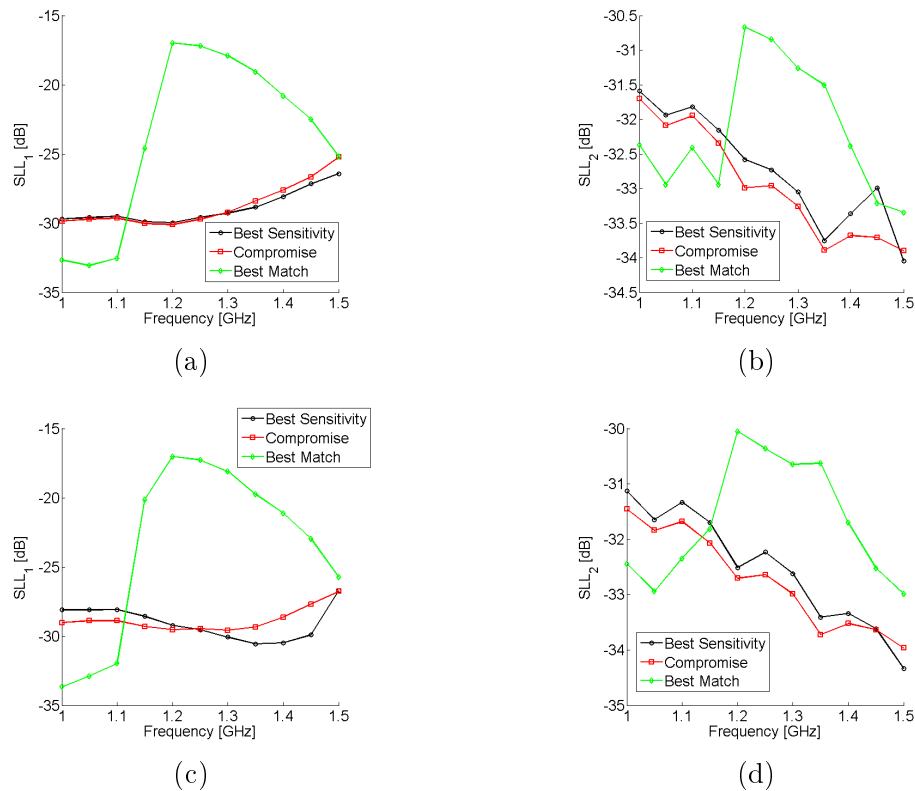


Figure 5.31: The SLLs over frequency of the secondary pattern for both two and three dimensional example solutions are shown. (a) SLL₁ and (b) SLL₂ of the two dimensional solutions. (c) SLL₁ and (d) SLL₂ of the three dimensional solutions. The best sensitivity solutions S_2 and S_3 are represented by black traces while the compromise solutions C_2 and C_3 are represented by red traces and the best match solution M_2 and M_3 are represented by green traces.

5.4.4 Conclusion

The Kriging interpolate based surrogate modelling investigated here was an attempt to find a means of performing a multi-objective optimisation of a problem that did not have particularly fast models available, namely the feed of a dual reflector system. At the simplest level, the surrogate could simply constitute an interpolate through fine model data. Alternatively, if a faster coarse model was available this could be used to build an interpolate that could then be partially corrected using a regression model. Both these were tried here through surrogates for the reflection coefficient that simply used S_{11} data extracted directly from a full wave simulation and sensitivity that used a full secondary pattern noise integration as the fine model and a main reflector masking technique as the coarse model. For the optimisation an iterative process was proposed where by after the initial optimisation the Pareto set was sampled for validation through comparison with fine model evaluations. If significant error was found then the surrogates would be reconstructed incorporating the data from the validation set.

These surrogates were applied to the general feed horn design discussed in Section 2.2.3.

Initially, a horn with a stepped matching section was investigated using a two dimensional solution space but this very quickly showed a generally poor reflection coefficient performance over the solution space. This surrogate did show a high degree of accuracy and needed only the initial construction and optimisation. Unfortunately, the optimisation did show that the solution space needed to be extended which was not feasible at the time. A second horn using a tapered matching section was also investigated. This was done for two and three dimensional solution space to get a feel for how this modelling technique coped with increasing solution space dimensionality. Again the surrogate showed a high degree of accuracy which unfortunately meant that the iterative step was not tested.

From these optimisations the worth of using this surrogate method for optimisation was concretely shown when looking at the number of function evaluations. The two dimensional solution spaces contained 2^{20} possible solutions with regard to the optimisation because of the 10 bit encoding used. For both cases approximately 14000 surrogate evaluations were performed compared to 441 coarse model and 5 fine model evaluation to construct the surrogate. Additionally, the optimisation took on the order of minutes to run. If the coarse model had been used directly by the optimiser, and assuming a similar number of function evaluations, this would have taken a little over a week and a half while if the fine model was used the optimisation would of taken well over four months. Illustrating this further, the three dimensional solution space contained 2^{30} possible solutions and the optimisation performed approximately 38000 surrogate evaluations in the order of minutes. A similar number of coarse model evaluations this would have taken over a month and using the fine model would have taken approximately a year. Even when factoring in approximately a day of simulation time to create the initial data sets and a day to condition the data and create the surrogates the difference in optimisation time is staggering.

Investigating the results of the optimisations showed that for the most part the the different solutions performed fairly similarly. In terms of a good general receiver for radio astronomy around 1.4 GHz S_3 was arguably the best of the solutions looked at in detail. Though this solution showed similar mean values to those of S_1 and S_2 it also showed a generally smoother response. This was even more true when compared to the sensitivity response of the remaining solutions. Additionally, despite having a maximum reflection coefficient above -20 dB, S_3 actually had -30 dB reflection coefficient over a significant portion of the band. This beats all but M_2 and M_3 . Finally, S_3 showed an SLL_1 under -25 dB and an SLL_2 under -30 dB that was stable over frequency. This was common to the other solution except for M_2 and M_3 . Interestingly, S_3 did not perform quite as well in terms of aperture efficiency and reflection coefficient when compared to the horn design by Lehmensiek and de Villiers [5]. This was also a three axial choke

horn designed for a similar band but used a two step matching section. The lower aperture efficiency could be attributed to the fact that S_1 was optimized for sensitivity while the horn in [5] was optimised for aperture efficiency. Using sensitivity may have caused slight under-illumination of the aperture to trade aperture efficiency for improved antenna temperature.

Chapter 6

Discussion

This study aimed to investigate the potential of two surrogate modelling techniques for use in the design and optimisation of a feed horn antenna for a dual Gregorian reflector system.

The first surrogate modelling technique investigated was space mapping (SM). It was applied to model aperture efficiency and showed some potential during single frequency alignment tests. These showed that part of the strength of SM was that the choice of SM parameter could often be linked to a physical aspect of the structure being designed that was misrepresented by the coarse model. The test also showed the importance of keeping this in mind when using SM, as a poor choice could actually be counter productive. SM base optimisation was hampered by the lack of a coarse model that was sufficiently faster than the fine model which meant that in general it was slower than simply using the fine model directly. This issue led to SM being abandoned for the purposes of this study. For SM to become a viable strategy, a fast approximation of the primary pattern would be needed.

The second surrogate modelling technique that was proposed was based around Kriging interpolation. This technique worked well producing stable Pareto fronts with errors in the validation sets of under 1 % for both the sensitivity and reflection coefficient. The grid sampling strategy worked well for the smooth response surfaces seen and all three optimisations showed the interpolate to be well converged with the initial surrogate construction. This did unfortunately mean that the surrogate realignment strategy was not required and could not be properly tested. Using the mean of the sensitivity over frequency led to the difference between the coarse and fine response becoming very small, in the region of 0.5 % of the peak sensitivity. The close alignment of the fine and coarse model was helpful for the surrogate construction it made it hard to fully gauge the contribution of the regression model between iterations.

This technique showed a significant reduction in time taken to produce the Pareto set.

After factoring in the simulation of the data sets the time taken to generate the Pareto front is estimated to be a little over a day. It must be noted that this not purely computation time and includes moving data around and conditioning data sets. Still this was a considerable improvement on the lowest estimate of over a week and a half for an optimisation using the coarse model directly.

A deeper investigation of a few example solutions showed that most exhibited very similar performance in terms of sensitivity, reflection coefficient, and SLL. The best sensitivity solution from the three dimensional solution space was deemed the the best solution by a marginal degree due to showing slightly more stable pattern characteristics and very good reflection coefficient for a large portion of the band. These also showed that a consistent -30 dB reflection coefficient was possible with a single tapered matching section it came at the cost of reduced sensitivity and significantly raised SLL_1 . Additionally comparing these solutions to previous work showed that this technique produced solutions that were approaching the performance of a design that was more complex in terms of matching section and the number of design parameters used.

There is still considerable scope for further study. The optimisation of higher dimensional solution spaces should to be attempted with the interpolation technique. This would allow for the iterative realignment strategy be tested as well as exploring the limits of the actual interpolation. Related to this, more complex data reduction method could be applied to the frequency dependant data before interpolation such as frequency masks. This could allow for finer control on the fitness assignment and take more frequency dependant characteristics into account which may lead to better quality solutions in the Pareto front. Finally there may be value in automating the whole iterative process but this is likely not to be entirely straight forward. Controls would have to be put in place to guide the surrogate realignment when the validation set is tightly limited to a small region of the solution space as this could cause the interpolate to degenerate.

List of References

- [1] C. A. Balanis, *Modern Antenna Handbook*. Wiley-Interscience, 2008.
- [2] A. Zhou, B.-Y. Qu, H. Li, S.-Z. Zhao, P. N. Suganthan, and Q. Zhang, “Multiobjective evolutionary algorithms: A survey of the state of the art,” *Swarm and Evolutionary Computation*, vol. 1, no. 1, pp. 32–49, 2011.
- [3] J. Bandler, R. Biernacki, S. H. Chen, P. Grobelny, and R. Hemmers, “Space mapping technique for electromagnetic optimisation,” *IEEE Transactions on Microwave Theory and Techniques*, vol. 42, no. 12, pp. 2536–2544, Dec 1994.
- [4] D. G. Krige, *A Statistical Approach to Some Mine Valuation and Allied Problems on the Witwatersrand*. publisher not identified, 1951.
- [5] R. Lehmensiek and D. de Villiers, “Wide flare angle axially corrugated conical horn design for a classical offset dual-reflector antenna,” in *2012 6th European Conference on Antennas and Propagation (EUCAP)*, Prague, Czech Republic, March 2012, pp. 3292–3294.
- [6] W. V. Rusch, A. Prata Jr, Y. Rahmat-Samii, and R. A. Shore, “Derivation and application of the equivalent paraboloid for classical offset Cassegrain and Gregorian antennas,” *IEEE Transactions on Antennas and Propagation*, vol. 38, pp. 1141–1149, 1990.
- [7] Y. Mizugutch, M. Akagawa, and H. Yokoi, “Offset dual reflector antenna,” in *1976 Antennas and Propagation Society International Symposium*, vol. 14, Amherst, Massachusetts, USA, Oct 1976, pp. 2–5.
- [8] C. Granet, “Designing classical offset cassegrain or gregorian dual-reflector antennas from combinations of prescribed geometric parameters,” *IEEE Antennas and Propagation Magazine*, vol. 44, no. 3, pp. 114–123, Jun 2002.
- [9] A. D. Olver, *Microwave Horns and Feeds*, ser. Electromagnetic Waves. Institution of Engineering and Technology, 1994.
- [10] R. Lehmensiek and I. Theron, “The design of the MeerKAT L-band feed,” in *2012 International Conference on Electromagnetics in Advanced Applications*, Cape Town,

- South Africa, Sept 2012, pp. 321–324.
- [11] Computer Simulation Technology, “CST STUDIO SUITE.” [Online]. Available: <https://www.cst.com/>
- [12] C. Balanis, *Antenna Theory: Analysis and Design*, ser. Antenna Theory: Analysis and Design. John Wiley & Sons, 2005, no. v. 1.
- [13] J. Kraus, *Radio astronomy*. Cygnus-Quasar Books, 1984.
- [14] J. Wrobel and R. Walker, “Sensitivity,” in *Synthesis Imaging in Radio Astronomy II*, vol. 180, 1999, p. 171.
- [15] P.-S. Kildal, “Factorization of the feed efficiency of paraboloids and Cassegrain antennas,” *IEEE Transactions on Antennas and Propagation*, vol. 33, pp. 903–908, Aug. 1985.
- [16] Z. Kildal, Per-Simon and Šipuš, “Classification of rotationally symmetric antennas as types BOR0 and BOR1,” *IEEE Antennas and Propagation Magazine*, vol. 37, no. 6, pp. 114–117, 1995.
- [17] W. Rusch and P. Potter, *Analysis of reflector antennas*. Academic Press, 1970.
- [18] R. Collin, “Aperture efficiency for paraboloidal reflectors,” *IEEE Transactions on Antennas and Propagation*, vol. 32, pp. 997–1000, 1984.
- [19] J. Yang, S. Pivnenko, and P.-S. Kildal, “Comparison of two decade-bandwidth feeds for reflector antennas: The eleven antenna and quadridge horn,” in *2010 4th European Conference on Antennas and Propagation (EUCAP)*, Barcelona, Spain, April 2010, pp. 1–5.
- [20] TICRA, “GRASP.” [Online]. Available: <http://www.ticra.com>
- [21] D. de Villiers *et al.*, “Offset dual-reflector antenna system efficiency predictions including subreflector diffraction,” *IEEE Antennas and Wireless Propagation Letters*, vol. 10, pp. 947–950, 2011.
- [22] D. de Villiers and R. Lehmensiek, “Rapid calculation of antenna noise temperature in offset Gregorian reflector systems,” *IEEE Transactions on Antennas and Propagation*, vol. 63, no. 4, pp. 1564–1571, April 2015.
- [23] W. A. Imbriale, “Faster antenna noise temperature calculations using a novel approximation technique,” in *2010 IEEE Antennas and Propagation Society International Symposium*, Toronto, Ontario, Canada, July 2010.
- [24] S. Koziel, J. Bandler, and K. Madsen, “A space-mapping framework for engineering optimisation - theory and implementation,” *IEEE Transactions on Antennas and Propagation*, vol. 54, no. 10, pp. 3721–3730, Oct 2006.

- [25] The MathWorks Inc., “Matlab.” [Online]. Available: <http://www.mathworks.com>
- [26] E. Zitzler, M. Laumanns, and S. Bleuler, “A tutorial on evolutionary multiobjective optimisation,” in *Metaheuristics for Multiobjective Optimisation*. Springer, 2004, pp. 3–37.
- [27] K. Deb, “Multi-objective genetic algorithms: Problem difficulties and construction of test problems,” *Evolutionary Computation*, vol. 7, no. 3, pp. 205–230, 1999.
- [28] S. Bureerat and K. Sriwornamas, “Population-based incremental learning for multiobjective optimisation,” in *Soft Computing in Industrial Applications*, ser. Advances in Soft Computing, A. Saad, K. Dahal, M. Sarfraz, and R. Roy, Eds. Springer Berlin Heidelberg, 2007, vol. 39, pp. 223–232.
- [29] S. Baluja, “Population-based incremental learning: A method for integrating genetic search based function optimisation and competitive learning,” Pittsburgh, PA, USA, Tech. Rep., 1994.
- [30] E. Zitzler, K. Deb, and L. Thiele, “Comparison of multiobjective evolutionary algorithms: Empirical results,” *Evolutionary Computation*, vol. 8, no. 2, pp. 173–195, 2000.
- [31] P.-S. Kildal, “Combined E- and H-plane phase centers of antenna feeds,” *IEEE Transactions on Antennas and Propagation*, vol. 31, no. 1, pp. 199–202, 1983.
- [32] M. D. McKay, R. J. Beckman, and W. J. Conover, “Comparison of three methods for selecting values of input variables in the analysis of output from a computer code,” *Technometrics*, vol. 21, no. 2, pp. 239–245, 1979.
- [33] J. Bandler, Q. Cheng, S. Dakroury, A. Mohamed, M. Bakr, K. Madsen, and J. Sondergaard, “Space mapping: the state of the art,” *IEEE Transactions on Microwave Theory and Techniques*, vol. 52, no. 1, pp. 337–361, Jan 2004.
- [34] A Matlab Kriging Toolbox, H. Nielsen, S. Lophaven, H. B. Nielsen, and J. Søndergaard, “Dace - a matlab kriging toolbox,” 2002.
- [35] P. Potter, *A new horn antenna with suppressed sidelobes and equal bandwidths*. Jet Propulsion Laboratory, California Institute of Technology, 1963.

Appendix A

Tables

Table A.1: Default horn parameters with all factors set to 1.

a_i	117.1 mm
N_{slots}	3
λ	239.8 mm
p	29.98 mm
w	23.98 mm
a_{t1}	141.1 mm
a_{t2}	165.1 mm
a_{t3}	189.1 mm
d_{t1}	66.75 mm
d_{t1}	65.59 mm
d_{t1}	64.75 mm
D	117.1 mm
L	234.2 mm

Table A.2: Validation set results for the two dimensional solution space optimisation of the stepped horn from Section 5.3.3.

D_f	L_f	Sensitivity			Match		
		Surrogate	Fine	% Error	Surrogate	Fine	% Error
1.0743	0.9851	4.4905	4.4781	0.2784	-18.7202	-18.4420	0.3771
1.0880	0.9906	4.4843	4.4822	0.0465	-19.0534	-18.4130	0.8532
1.1067	0.9844	4.4809	4.4510	0.6713	-19.5339	-19.4853	0.0592
1.1146	0.9844	4.4699	4.4309	0.8809	-19.8798	-19.5810	0.3549
1.1185	0.9828	4.4568	4.4292	0.6248	-20.0992	-19.6983	0.4671
1.1216	0.9820	4.4426	4.4392	0.0774	-20.2733	-19.9859	0.3261
1.0731	0.5855	4.4296	4.4363	0.1505	-20.4956	-19.7720	0.8206
1.1294	0.9914	4.4072	4.4186	0.2584	-20.6880	-20.5850	0.1102
1.1333	0.9937	4.3913	4.3793	0.2752	-20.8584	-20.8188	0.0414
1.1388	0.9914	4.3712	4.3552	0.3670	-20.9724	-20.4207	0.5863

APPENDIX A. TABLES

Table A.3: Validation set results for the two dimensional solution space optimisation of the tapered horn from Section 5.4.1.

D_f	L_f	Sensitivity			Match		
		Surrogate	Fine	% Error	Surrogate	Fine	% Error
1.0821	0.9844	4.4853	4.4705	0.3329	-19.2069	-19.3910	0.2297
1.1079	0.9797	4.4784	4.4667	0.2620	-19.9869	-20.3698	0.4319
1.1109	0.5761	4.4651	4.4663	0.0282	-20.3848	-20.2422	0.1584
1.1191	0.7177	4.4598	4.4572	0.0577	-20.7425	-20.3511	0.4231
1.1320	0.6528	4.4506	4.4495	0.0266	-21.0578	-21.0659	0.0082
1.1425	0.5793	4.4415	4.4411	0.0085	-21.3590	-21.2819	0.0762
1.1484	0.5816	4.4342	4.4332	0.0234	-21.6779	-21.4760	0.1938
1.1548	0.5980	4.4240	4.4215	0.0565	-22.0067	-21.6891	0.2956
1.1578	0.6066	4.4184	4.4156	0.0633	-22.1184	-21.9275	0.1741
1.1630	0.6113	4.4084	4.4056	0.0628	-22.2294	-22.1573	0.0645
1.1677	0.6152	4.3982	4.3895	0.1987	-22.2734	-21.8845	0.3524
1.1724	0.6137	4.3878	4.3821	0.1293	-22.2999	-22.2433	0.0501
1.1877	0.5144	4.3768	4.3738	0.0687	-22.4192	-22.0097	0.3654
1.1947	0.5050	4.3659	4.3655	0.0104	-22.7134	-22.4496	0.2257
1.5848	0.2211	4.3218	4.3098	0.2776	-32.2926	-31.4999	0.2321

Table A.4: Validation set results for the three dimensional solution space optimisation of the tapered horn From Section 5.4.2.

θ_{flare}	D_f	L_f	Sensitivity			Match		
			Surrogate	Fine	% Error	Surrogate	Fine	% Error
15.5425	1.1625	0.2274	4.4930	4.4789	0.3158	-18.9170	-19.0455	0.1663
18.7097	1.1736	0.2321	4.4884	4.4810	0.1660	-19.4065	-19.3203	0.1068
26.9208	1.1167	0.9718	4.4753	4.4554	0.4462	-20.2699	-20.1615	0.1217
26.3930	1.1220	0.5754	4.4672	4.4654	0.0412	-20.5453	-20.7073	0.1735
25.5718	1.1314	0.5730	4.4613	4.4597	0.0345	-20.8991	-20.9285	0.0305
26.2170	1.1343	0.5769	4.4583	4.4561	0.0505	-21.0429	-21.0501	0.0074
26.5103	1.1378	0.5699	4.4555	4.4539	0.0369	-21.1619	-21.2741	0.1123
26.8035	1.1413	0.5824	4.4507	4.4474	0.0728	-21.3586	-21.4178	0.0581
26.9208	1.1455	0.5746	4.4468	4.4424	0.1008	-21.4881	-21.4587	0.0285
26.5103	1.1496	0.5808	4.4417	4.4354	0.1415	-21.6523	-21.6015	0.0485
27.0381	1.1531	0.5855	4.4358	4.4305	0.1199	-21.8121	-21.6976	0.1077
26.9208	1.1572	0.5863	4.4298	4.4240	0.1309	-21.9490	-22.0013	0.0480
26.9795	1.1619	0.5801	4.4232	4.4160	0.1630	-22.0828	-22.0969	0.0128
27.7419	1.1642	0.5761	4.4184	4.4145	0.0889	-22.1722	-22.3353	0.1449
27.5073	1.1660	0.5801	4.4151	4.4113	0.0855	-22.2305	-22.3261	0.0846
27.9179	1.1689	0.5738	4.4099	4.4029	0.1591	-22.3177	-22.2646	0.0469
27.5073	1.1718	0.5801	4.4038	4.3952	0.1944	-22.4069	-22.3117	0.0835
28.0938	1.1742	0.5754	4.3985	4.3911	0.1690	-22.4883	-22.4788	0.0083
18.4751	1.3695	0.2149	4.3875	4.3820	0.1258	-23.2369	-22.6932	0.4450
33.4897	1.5877	0.2055	4.3265	4.3179	0.2004	-32.1466	-32.1977	0.0145

Appendix B

Feed Profiles

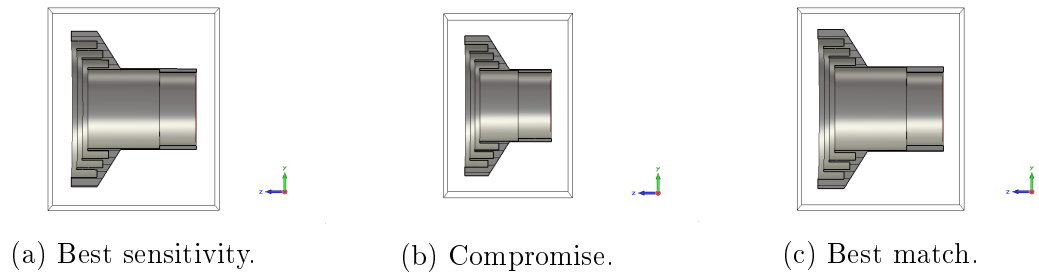


Figure B.1: Stepped profile examples from the two dimensional validation set in Section 5.3.3.

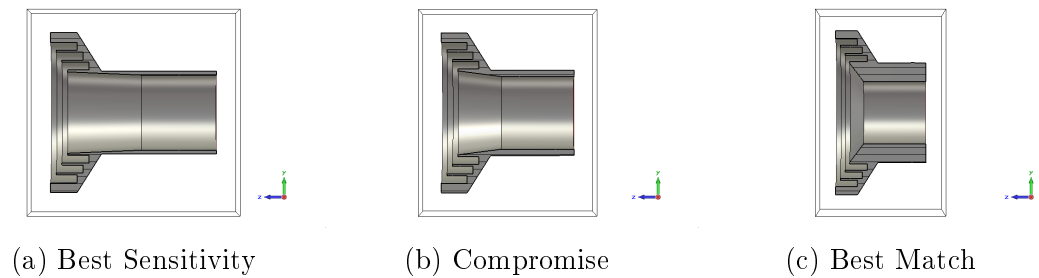


Figure B.2: Tapered profile examples from the two dimensional validation set in Section 5.4.1

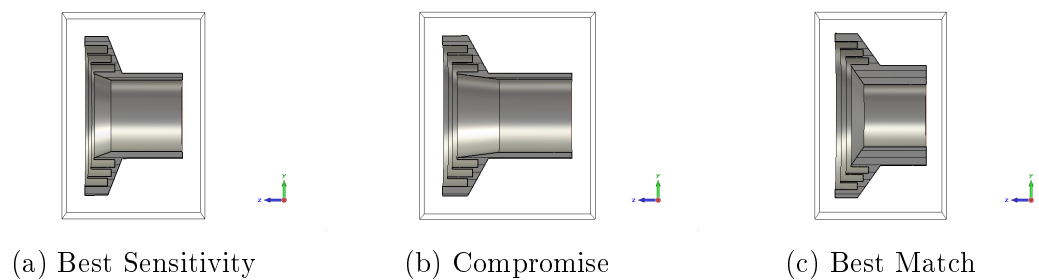


Figure B.3: Tapered profile examples from the three dimensional validation set in Section 5.4.2